Astronomy & Astrophysics manuscript no. sn2011dh-2-no-hydro-v2
March 17, 2014

The type IIb SN 2011dh - 2 years of observations and modelling of the bolometric and photometric lightcurves.

M. Ergon[1], A. Jerkstrand[2] **Group 1 (in alphabetic order):**, M. Bersten[6], N. Elias-Rosa[5], C. Fransson[1], M. Fraser[2], A. Pastorello[3], J. Sollerman[1], S. Taubenberger[4], S. Valenti[7,8] **Group 2 (in alphabetic order, to be extended):**, S. Benetti[3], S. Smartt[2], and L. Tomasella[3]

[1] The Oskar Klein Centre, Department of Astronomy, AlbaNova, Stockholm University, 106 91 Stockholm, Sweden
[2] Astrophysics Research Center, School of Mathematics and Physics, Queens University Belfast, Belfast, BT7 1NN, UK
[3] INAF, Osservatorio Astronomico di Padova, vicolo dell'Osservatorio n. 5, 35122 Padua, Italy
[4] Max-Planck-Institut für Astrophysik, Karl-Schwarzschild-Str. 1, D-85741 Garching, Germany
[5] Institut de Ciències de l'Espai (IEEC-CSIC), Facultat de Ciències, Campus UAB, E-08193 Bellaterra, Spain.
[6] Kavli Institute for the Physics and Mathematics of the Universe, Todai Institutes for Advanced Study, University of Tokyo, 5-1-5 Kashiwanoha, Kashiwa, Chiba 277-8583, Japan
[7] Las Cumbres Observatory Global Telescope Network, 6740 Cortona Dr., Suite 102, Goleta, CA 93117, USA
[8] Department of Physics, University of California, Santa Barbara, Broida Hall, Mail Code 9530, Santa Barbara, CA 93106-9530, USA

Submitted to Astronomy and Astrophysics

ABSTRACT

We present optical and near-infrared (NIR) photometry and spectroscopy of the Type IIb supernova (SN) 2011dh spanning 2 years, and modelling of the bolometric and photometric lightcurves. To model the 0-100 days bolometric lightcurves of SNe 2011dh, 1993J and 2008ax, we use the hydrodynamical model grid and the fitting procedure presented in Ergon et al. (2014a), which allows us to determine the errors in the derived quantities. Using this method we find a helium core mass of $3.4^{+0.6}_{-0.3}$ $M_\odot$ for SN 2011dh and similar values for SNe 1993J and 2008ax. Using a bolometric correction determined with steady-state NLTE modelling we extend the temporal coverage of the model grid to 300 days and applied to SN 2011dh we obtain results in good agreement with those based on the 0-100 days bolometric lightcurve. We present 100-500 days bolometric and photometric lightcurves for the Jerkstrand et al. (2014) steady-state NLTE models and discuss the constraints derived from the those on the model parameters. The optimal 12 $M_\odot$ model, presented and found to give a good agreement with observed nebular spectra in Jerkstrand et al. (2014), shows a good agreement with the observed lightcurves, although the evolution in the MIR is only partly reproduced. Time-dependent NLTE modelling shows that after 600 days a steady-state assumption is no longer valid. The radioactive energy deposition in this phase is likely dominated by the positrons emitted in the decay of ^{56}Co but what energy source is dominating the emitted flux is unclear. We find an excess in the MIR developing between 100 and 200 days, during which an increase in the optical tail decline rates is also observed. Steady-state NLTE models with a modest amount of dust (τ = 0.25) added during this period partly reproduce this behaviour. A modest amount of CO first overtone band emission is detected at 89 and 202 days implying a contribution to the Spitzer 4.5 μm band from CO fundamental band emission. Examining the steady-state NLTE models neither complete CO cooling nor abscence of CO cooling in the C/O zone well reproduce the observed Spitzer 4.5 μm flux suggesting an intermediate scenario. Estimates of the sizes of the line emitting regions, ranging from ~3000 km s^{-1} for the oxygen lines to ~1500 km s^{-1} for the iron lines, suggest partial mixing of the nuclear burning zones, and the sizes of these regions are in all compared cases smaller than for SNe 1993J and 2008ax. The profiles of the [O I] 6300 Å and Mg I] 4571 Å lines show a remarkable similarity, suggesting these lines to be emitted by the same material and to originate from the O/Ne/Mg zone. We use repetitions of small scale fluctuations in the [O I] 6300 Å and [O I] 6364 Å lines to estimate a line ratio close to 3, consistent with optically thin emission, from 200 days and onwards. This paper concludes our extensive observational and modelling work on SN 2011dh presented in a series of papers. The results from hydrodynamical modelling, steady-state NLTE modelling and stellar evolutionary progenitor analysis presented in Maund et al. (2011), Bersten et al. (2012), Jerkstrand et al. (2014) and this paper are all consistent and suggest an initial mass of ~13 $M_\odot$ for the progenitor. The initial masses of $\lesssim$15 $M_\odot$ found for SNe 2011dh, 1993J and 2008ax, by hydrodynamical modelling and steady-state NLTE modelling in Jerkstrand et al. (2014) and this paper suggest that all of these Type IIb SNe originates from binary systems, as previously established for SN 1993J.

Key words. supernovae: general — supernovae: individual (SN 2011dh) — galaxies: individual (M51)

1. Introduction

Type IIb supernovae (SNe) are observationally characterized by a transition from Type II (with hydrogen lines) at early times to Type Ib (without hydrogen lines but with helium lines) at later times. The physical interpretation is that these SNe arise from stars that have lost most of their hydrogen envelope, either through stellar winds or interaction with a binary companion. Which of these production channels are dominating is still debated but for SN 1993J, the prime example of such an SN, a companion star was detected by direct observations (Maund et al. 2004). The evolution of this binary system has been successfully modelled (Podsiadlowski et al. 1993; Stancliffe & El-

dridge 2009) and it is widely accepted that the companion was responsible for the removal of the hydrogen envelope. Bright, nearby Type IIb SNe as 1993J, 2008ax and the recent 2011dh are essential to improve our understanding of this class. Observations of the progenitor star in pre-explosion images, a search for the companion star when the SN has faded and multi-method modelling of high quality data, all provide important clues to the nature of Type IIb SNe and their progenitor stars.

In this paper we present the extensive optical and near-infrared (NIR) dataset, covering nearly two years, that we have obtained for SN 2011dh. The first 100 days of this dataset have been presented in Ergon et al. (2014b, herafter E14a). Detailed hydrodynamical modelling of the SN using those data were presented in Bersten et al. (2012, hereafter B12) and steady-state NLTE modelling of nebular spectra in Jerkstrand et al. (2014, hereafter J14). Identification and analysis of the plausible progenitor star was presented in Maund et al. (2011, hereafter M11) and confirmation of the progenitor identification through its disappearance in E14a.

SN 2011dh was discovered on 2011 May 31.893 UT (Griga et al. 2011) in the nearby galaxy M51 at a distance of 7.8 Mpc (E14a). The SN has been extensively monitored from X-ray to radio wavelengths by several teams. Most observations cover the 3-100 days period, but late time data have been published in Tsvetkov et al. (2012), Van Dyk et al. (2013), Sahu et al. (2013), Shivvers et al. (2013) and Helou et al. (2013). As in E14a we focus on the UV to MIR emission. The explosion epoch, the distance to M51 and the interstellar line-of-sight extinction towards the SN used in this paper, are all adopted from E14a.

The nature of the progenitor star has been a key issue since the identification of a yellow supergiant in pre-explosion images, coincident with the SN (M11; Van Dyk et al. 2011). Recent progress in modelling of the SN (B12; J14; Shivvers et al. 2013) and the disappearance of the progenitor candidate (E14a; Van Dyk et al. 2013) strengthens the hypothesis that the progenitor was a yellow supergiant of moderate mass, as was originally proposed in M11. In this paper we present further modelling in support of this hypothesis. As shown in Benvenuto et al. (2013) a binary interaction scenario that reproduces the observed and modelled properties of the yellow supergiant is possible. HST observations that could detect or set useful constraints on the presence of a companion star are scheduled for Cycle 21.

The paper is organized as follows. In Sect. 2 we present the observations and describe the reduction and calibration procedures and in Sect. 3 we present an observational analysis and comparison of the observations to SNe 1993J and 2008ax. In Sect. 4 we model the bolometric and photometric lightcurves and in Sect. 5 we discuss the interpretation of the observations given our optimal model and discuss and review the results obtained so far and our current understanding of Type IIb SNe. Finally, we conclude and summarize the paper in Sect. 6. In Appendix **??** we provide details on the hydrodynamical modelling.

2. Observations

2.1. Software

As in E14a two different software packages have been used for 2-D reductions, measurements and calibrations of the data. The IRAF based QUBA pipeline (Valenti et al. 2011, hereafter V11) and another IRAF based package which we will refer to as the SNE pipeline. This package has been developed with the particular aim to provide the high level of automation needed for large sets of data.

2.2. Imaging

An extensive campaign of optical and NIR imaging was initiated for SN 2011dh shortly after discovery using a multitude of different instruments. The observations during the first 100 days have been described in E14a. The late time data were obtained with the Liverpool Telescope (LT), the Nordic Optical Telescope (NOT), Telescopio Nazionale (TNG), the Calar Alto 3.5m (CA 3.5m) and 2.2m (CA 2.2m) telescopes, the Asiago 67/92cm Schmidt (AS Schmidt) and 1.82m Copernico (AS 1.82m) telescopes, the William Herschel Telescope (WHT), the Albanova Telescope (AT) and the United Kingdom Infrared Telescope (UKIRT). The major contributors were the NOT, the AS Schmidt and the AT for the optical observations and the the CA 3.5m, the WHT and the UKIRT for the NIR observations. The late time dataset includes 61 epochs of optical imaging and 9 epochs of NIR imaging which, together with the early time observations, gives a total of 146 epochs of optical imaging and 32 epochs of NIR imaging.

2.2.1. Reductions and calibration

The optical and NIR raw data have been reduced with the QUBA and SNE packages respectively as described in E14a, except for the optical LT and NIR UKIRT data for which reductions provided by the automated telescope pipelines have been used. Photometry was performed with the SNE pipeline as described in E14a. Comparison to photometry on template subtracted images shows that the background contamination is negligible before ~300 days after which we have used photometry on template subtracted images. The optical and NIR photometry was calibrated to the Johnson-Cousins (JC), Sloan Digital Sky Survey (SDSS) and 2 Micron All Sky Survey (2MASS) systems as described in E14a where we also discuss the related uncertainties. The photometry was transformed to the standard systems using S-corrections (Stritzinger et al. 2002) as described in E14a, except for the JC *U* and SDSS *u* bands which were transformed using the linear colour-terms tabulated in E14a. As discussed in E14a we find the calibration to be accurate to within five percent in all bands for the first 100 days. The accuracy of the late time photometry depends critically on the accuracy of the S-corrections. The late time JC and SDSS photometry were mainly obtained with the NOT but comparisons between S-corrected NOT, LT and CA 2.2m JC and SDSS observations at ~300 days show differences at the 5 percent level suggesting that this precision is maintained. We note that in this phase S-corrections are absolutely necessary. For example the difference between the NOT and CA 2.2m *I* band observations are almost one magnitude at ~300 days if these are not applied, mainly because of the strong [Ca II] 7291,7323 Å and Ca II 8498,8542,8662 Å lines. The late time 2MASS photometry was obtained with a number of different telescopes and although the sampling is sparse the shape of the lightcurves suggests that the errors in the S-corrections are modest. Note that we have used JC-like *UBVRI* filters and SDSS-like *gz* filters at NOT whereas we have used JC-like *BV* filters and SDSS-like *ugriz* filters at LT. The JC-like *URI* and SDSS-like *uri* photometry were then tied to both the JC and SDSS systems to produce full sets of JC and SDSS photometry.

!We probably add a discussion here, or possible a separate section, on the very late time observations and the uncertainties in these.!

2.2.2. Space Telescope Observations

We have also performed photometry on the Spitzer 3.6 and 4.5 μm imaging[1] using the SNE pipeline as described in E14a to calculate magnitudes in the natural (energy flux based) Vega system of IRAC. All Spitzer images were template subtracted as described in E14a and the photometry is in good agreement with that published in Helou et al. (2013) !quantify this!. Optical and UV SWIFT magnitudes were published in E14a.

2.2.3. Results

The S-corrected optical and NIR magnitudes and their corresponding errors are listed in Tables 4, 5 and 6 and the Spitzer 3.6 and 4.5 μm magnitudes and their corresponding errors in Table 7. For completeness we also include the magnitudes for the first 100 days already published in E14a. All magnitudes, including the SWIFT magnitudes published in E14a, are shown in Fig. 1 which also shows cubic spline fits using 3-5 point knot separation, error weighting and a 5 percent error floor or, when the sampling is sparse, linear interpolations as well as extrapolations assuming a constant colour to adjacent bands. All calculations in Sect. 3, including the construction of the bolometric lightcurve, are based on these spline fits, interpolations and extrapolations. In these calculations the errors in the fitted splines have been estimated as the standard deviation and then propagated.

2.3. Spectroscopy

An extensive campaign of optical and NIR spectroscopic observations was initiated for SN 2011dh shortly after discovery with data obtained from a multitude of telescopes. The observations during the first 100 days have been described in E14a. The late time data were obtained with the NOT, the TNG, the WHT, the CA 2.2m, the Asiago 1.22m Galileo telescope (AS 1.22m), and the Gran Telescopio Canarias (GTC). The major contributors were the NOT, the WHT and the GTC. Details of all spectroscopic observations, the telescope and instrument used, epoch and instrument characteristics are given in Table 8. The late time dataset includes 18 optical spectra obtained at 13 epochs and 2 NIR spectra obtained at 2 epochs which, together with the early time observations, gives a total of 73 optical spectra obtained at 39 epochs and 20 NIR spectra obtained at 12 epochs.

2.3.1. Reductions and calibration

The optical and NIR raw data were reduced and the flux extracted using the QUBA and SNE pipelines respectively as described in E14a. The optical and NIR spectra were flux and wavelength calibrated using the QUBA and SNE pipelines respectively as described in E14a. The absolute flux scale of all spectra has been calibrated against interpolated photometry using a least square fit to all bands for which the mean energy wavelength is at least half an equivalent width within the spectral range.

!Some spectra still has to be corrected for telluric absorption. The wavelength calibration of all spectra, with the important exception of the ∼200 days NIR spectra, have been checked against skylines but some have not been shifted yet (but in all these cases the shift is very small).!

[1] Obtained through the DDT program by G. Helou.

2.3.2. Results

All reduced, extracted and calibrated spectra will be made available for download from the Weizmann Interactive Supernova data REPository[2] (WISeREP) (Yaron & Gal-Yam 2012). Figure 3 shows the sequence of observed spectra where those obtained on the same night using the same telescope and instrument have been combined. For clarity some figures in this and the following sections are based on time-interpolations of the spectral sequence as described in E14a. To further visualize the evolution, the spectra have been aligned to a time axis at the right border of the panels. Interpolated spectra were used in the calculations of the bolometric lightcurve (Sect. 3.2) and S-corrections. Figure 2 shows the interpolated optical and NIR spectral evolution of SN 2011dh for 5−425 days with a 20-day sampling. All spectra in this and subsequent figures have been corrected for redshift and interstellar extinction.

3. Analysis

In this section we provide an analysis of the data and a comparison of these to the Type IIb SNe 1993J and 2008ax. Besides SN 2011dh, these are the best monitored Type IIb SNe so far, which motivates a detailed comparison. Both occurred in nearby galaxies, have progenitor detections and well constrained explosion epochs. We keep the analysis of the photometric and bolometric evolution observational, as we return to the physical interpretation in Sect. 4, where we present steady-state NLTE and hydrodynamical modelling of these data. The analysis of the spectral evolution is complementary to the steady-state NLTE modelling of these data in J14, and we therefore frequently refer to this paper and the results obtained therein. The early (0-100 days) evolution of SN 2011dh, as well as comparisons in this phase to SNe 1993J and 2008ax, were discussed in E14a, and here we focus on the evolution after 100 days.

As discussed in E14a, the systematic errors stemming from the uncertainties in distance and extinction are large for all three SNe, which should be kept in mind when absolute quantities are compared. For SNe 1993J and 2008ax we adopt the same values and error bars for the distance and extinction as in E14a. The references for the photometric and spectroscopic data of SNe 1993J and 2008ax used in the comparison are the same as specified in E14a !not true, we use additional late time data!. We note that the lack of S-corrected photometry for SN 1993J complicates the comparison, whereas for SN 2008ax the S-corrected JC photometry by Taubenberger et al. (2011) agrees reasonably well with the JC photometry by Tsvetkov et al. (2009).

3.1. Photometric evolution

Absolute magnitudes were calculated as in E14a. In Fig. 4 we show absolute optical and NIR magnitudes for SN 2011dh as compared to SNe 1993J and 2008ax, and in Table 1 we tabulate the tail decline rates at 100, 200 and 300 days. Most striking is the similarity between the lightcurves, except for a shift towards higher luminosities for SNe 1993J and 2008ax, the shift being larger in bluer bands and negligible in the NIR and most pronounced for SN 2008ax. As discussed in E14a, this difference could be explained by an error in the adopted extinctions.

Given the caveat that SNe 1993J and 2008ax are only partly covered in U and NIR, we find the following general trends. At 100 days the V, R and I decline rates are roughly twice the de-

[2] http://www.weizmann.ac.il/astrophysics/wiserep/

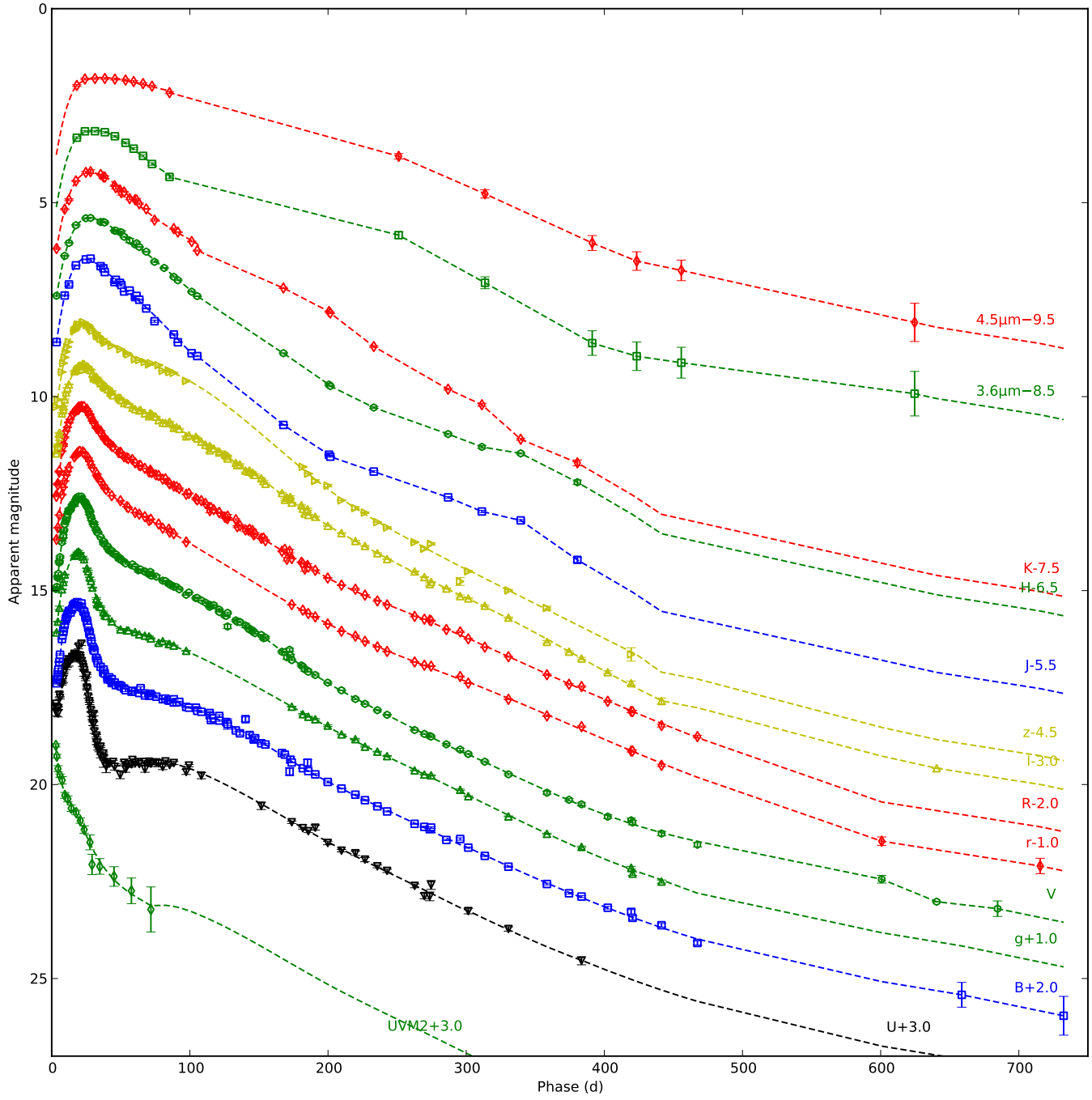

Fig. 1. Photometric evolution of SN 2011dh in the UV, optical, NIR and MIR. For clarity each band has been shifted in magnitude. Each lightcurve has been annotated with the name of the band and the shift applied. We also show combinations of spline fits, interpolations and extrapolations decribed in Sect 2.2.3 (dashed lines).

cay rate of ^{56}Co, and subsequently decrease towards 300 days. The *U* and *B* decline rates are significantly lower at 100 days, subsequently approach the other optical decline rates and then evolve similarly. The *J* and *H* band decline rates are considerably higher than the optical at 100 days, subsequently approaches those and eventually become considerably lower. For SNe 2011dh and 1993J the *K* band behaves quite differently than the other NIR bands. At 100 days the decline rate is significantly lower, but as it remains roughly constant, it subsequently approach the other NIR decline rates and eventually becomes condsiderably higher. As seen in Fig. 1, the optical lightcurves of SN 2011dh flatten considerably after ~450 days, approaching a decline rate similar to, or lower than, the decay rate of ^{56}Co.

Both SNe 2011dh and 1993J were also monitored in the MIR, SN 2011dh in the Spitzer 3.6 and 4.5 μm bands and SN 1993J in the *L* band, which is similar to the Spitzer 3.6 μm band. For both SNe a strong excess in the MIR develops between ~100 and ~250 days. For SN 1993J the MIR coverage ends at ~250 days and for SN 2011dh the subsequent evolution is fairly similar to the evolution in the optical, and the considerable flattening seen in the optical lightcurves after ~450 days, is also seen in the Spitzer lightcurves.

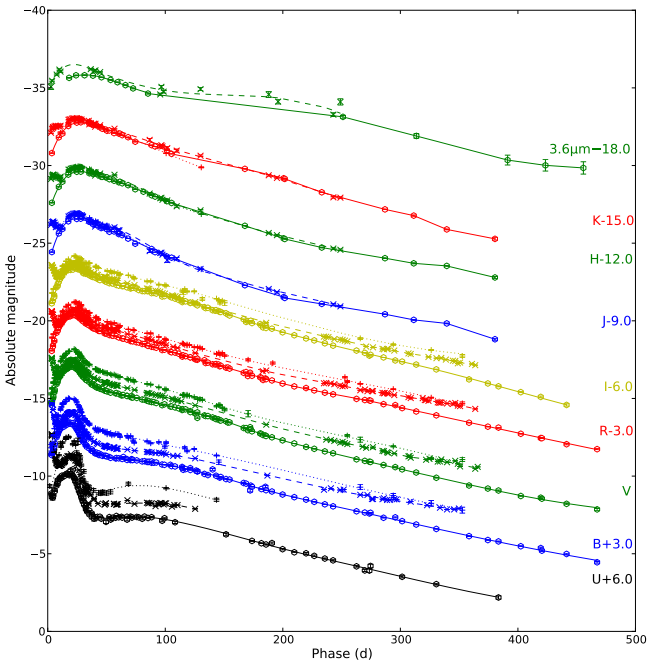

Fig. 4. Photometric evolution of SN 2011dh (dots) in the optical and NIR as compared to SNe 1993J (crosses) and 2008ax (pluses). For clarity each band has been shifted in magnitude. Each lightcurve has been annotated with the name of the band and the shift applied. We also show combinations of spline fits, interpolations and extrapolations described in Sect. 2.2.3 (dashed lines).

!I have removed a discussion on the colour evolution here. Maybe this should be included, I'm not sure. It is a very long paper.!

3.2. Bolometric evolution

As in E14a we have used a combination of the spectroscopic and photometric methods, applied to wavelength regions with and without spectral information respectively, when calculating the pseudo-bolometric lightcurves. The details of these methods have been described in E14a. Combinations of spline fits, interpolations and extrapolations, as decribed in Sect. 2.2.3 and shown in Figs. 1 and 4, have been used to calculate the magnitudes.

Figure 5 shows the U to K (3300-24000 Å) pseudo-bolometric lightcurves for SN 2011dh as compared to SNe 1993J and 2008ax for the 0-500 days period as calculated with the photometric method, and in Table 2 we tabulate the decline rates at 100, 200 and 300 days. Given the caveat that SNe 1993J and 2008ax are not covered in NIR after ~250 and ~150 days respectively, their U to K pseudo-bolometric lightcurves are remarkably similar to the one of SN 2011dh, except for the shift towards higher luminosities discussed previously in Sect. 3.1. The decline rates decrease from ~0.020 mag day^{-1}, roughly twice the decay rate of ^{56}Co, at 100 days to ~0.015 mag day^{-1} at 300 days. There is however a significant increase in the decline rate between ~150 and ~200 days for SN 2011dh, not seen for SNe 1993J and 2008ax. For SN 1993J the decline rate becomes increasingly lower towards 300 days as compared to SNe 2011dh and 2008ax, which is consistent with an increasing contribution from CSM interaction in this phase.

Figure 6 shows the UV to MIR (1900-50000 Å) pseudo-bolometric lightcurve for SN 2011dh, as calculated with the combined spectroscopic and photometric methods, and in Table 9 we tabulate the 3-300 days period (for which we have full UV to MIR coverage) for reference. As expected, the UV to MIR and U to K pseudo-bolometric lightcurves are very simi-

Table 1. Tail decline rates at 100, 200 and 300 days for SN 2011dh compared to SNe 1993J and 2008ax as measured from cubic spline fits.

SN	Band	Rate (100 d) (mag day^{-1})	Rate (200 d) (mag day^{-1})	Rate (300 d) (mag day^{-1})
2011dh	*U*	0.013	0.019	0.018
2011dh	*B*	0.014	0.019	0.017
2011dh	*V*	0.018	0.021	0.018
2011dh	*R*	0.020	0.019	0.016
2011dh	*I*	0.019	0.021	0.017
2011dh	*J*	0.036	0.017	0.012
2011dh	*H*	0.029	0.019	0.011
2011dh	*K*	0.020	0.020	0.024
1993J	*U*	0.006	...	...
1993J	*B*	0.011	0.017	0.012
1993J	*V*	0.019	0.019	0.017
1993J	*R*	0.022	0.015	0.013
1993J	*I*	0.022	0.019	0.013
1993J	*J*	0.041	0.016	...
1993J	*H*	0.033	0.018	...
1993J	*K*	0.023	0.022	...
2008ax	*U*	0.013	...	...
2008ax	*B*	0.015	0.018	0.016
2008ax	*V*	0.022	0.018	0.017
2008ax	*R*	0.023	0.016	0.015
2008ax	*I*	0.018	0.021	0.013
2008ax	*J*	0.035	...	...
2008ax	*H*	0.032	...	...
2008ax	*K*	0.033	...	...

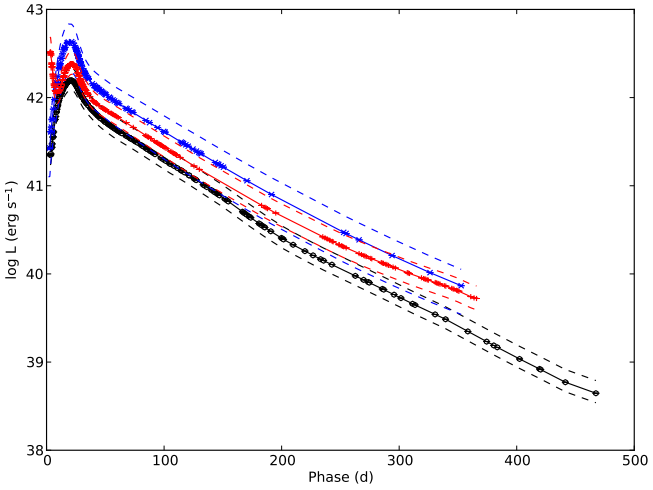

Fig. 5. Pseudo-bolometric U to K lightcurve for SN 2011dh (black circles and solid line) calculated with the photometric method as compared to SNe 1993J (red crosses and solid line) and 2008ax (blue pluses and solid line). The upper and lower error bars for the systematic error arising from extinction and distance (dashed lines) are also shown.

Table 2. Tail decline rates at 100, 200, and 300 days for the *U* to *K* bolometric lightcurve of SN 2011dh compared to SNe 1993J and 2008ax.

SN	Rate (100 d) (mag day^{-1})	Rate (200 d) (mag day^{-1})	Rate (300 d) (mag day^{-1})
2011dh	0.021	0.021	0.016
2008ax	0.020	0.017	0.015
1993J	0.021	0.017	0.013

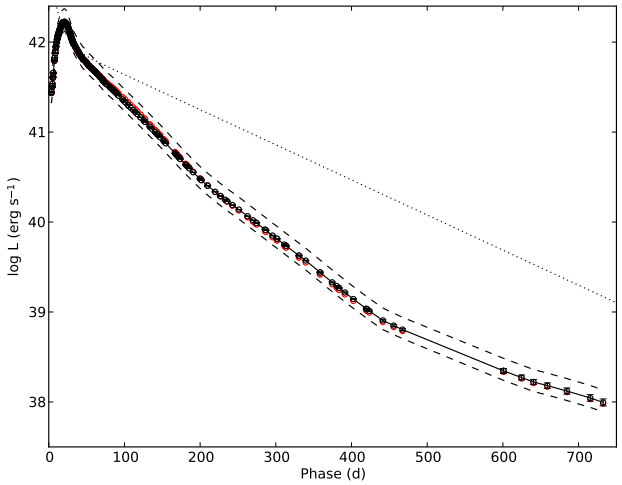

Fig. 6. Pseudo-bolometric UV to MIR lightcurve for SN 2011dh calculated with the spectroscopic (black circles and solid line) and photometric (red circles) method. The upper and lower error bars for the systematic error arising from extinction and distance (black dashed lines) and the radioactive decay chain luminosity of 0.075 $M_\odot$ of ^{56}Ni (black dotted line) are also shown.

lar. The decline rates at 100, 200, 300 and 400 days are 0.021, 0.022, 0.015 and 0.016 mag day^{-1}, but the increase in decline rate between ~150 and ~200 days is not as pronounced as in the *U* to *K* pseudo-bolometric lightcurve. Given the caveats that the NIR coverage ends at ~350 days, and the sampling is sparse and the measurement errors large after ~500 days, the UV to MIR pseudo-bolometric lightcurve shows a significant flattening after ~500 days, when the decline rate decreases to a value similar to, but lower than, the decay rate of ^{56}Co.

Figure 7 shows the fractional UV (1900-3300 Å), optical (3300-10000 Å), NIR (10000-24000 Å) and MIR (24000-50000 Å) luminosities for SN 2011dh. The early evolution was discussed in E14a, and after 100 days the most notable is the strong increase in the MIR fraction between ~100 and ~250 days. The subsequent evolution becomes quite uncertain after ~350 days when the NIR coverage ends and ~500 days when the sampling and measurement errors become worse, but the optical, NIR and MIR fractions seems to be roughly constant during this period. Keeping these uncertainties in mind it is worth noting the dominance of the optical flux even at ~750 days.

Figure 8 shows the evolution of the SED as calculated with the photometric method, overplotted with blackbody fits to the *V*, *I*, *J*, *H* and *K* photometry as well as the observed (interpolated) spectra. The early evolution was discussed in E14a, and after 100 days the most notable is again the strong excess de-

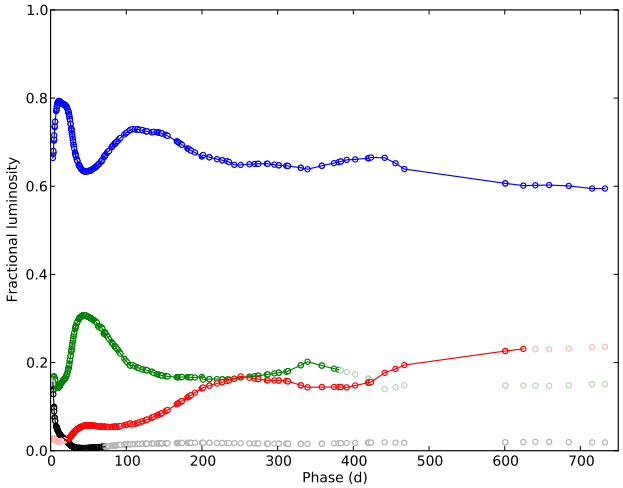

Fig. 7. Fractional UV (black dots), optical (blue dots), NIR (green dots) and MIR (red dots) luminosity for SN 2011dh. Luminosities based on extrapolated magnitudes are displayed in shaded colour.

veloping in the MIR between ~100 and ~250 days. There also seems to be a similar excess developing in the *K* band between ~100 and ~200 days, gradually fading away towards 300 days.

3.3. Spectroscopic evolution

The early spectral evolution was discussed in some detail in E14a and in this section we focus on the spectral evolution from 100 days and onwards. Steady-state NLTE modelling of this evolution as well as a detailed analysis of the formation of the identified lines and the evolution of their fluxes are presented in J14. In this section we summarize the findings in J14 and provide a complementary analysis, mainly related to the line profiles and what can be learned about the distribution of the material from the different nuclear burning zones. In doing this we refer to the subdivision of the (unmixed) ejecta described in J14 with a Fe/Co/He core surrounded by the Si/S zone, the oxygen-rich O/Si/S, O/Ne/Mg and O/C zones, the helium-rich He/C and He/N zones and the hydrogen-rich envelope. The amount of macroscopic mixing between these zones is determined by hydrodynamical instabilities in the explosion (Hammer et al. 2010) and is a free parameter in the steady-state NLTE modelling.

In Sect. 3.3.1 we describe our methods for characterization of the line profiles and estimation of the line emitting regions, in Sects. 3.3.2-3.3.8 we discuss the identified lines element by element, in Sect. 3.3.10 we discuss small scale variations in the line profiles and in Sect. 3.3.11 we compare the line profiles of SN 2011dh to those of SNe 1993J and 2008ax.

3.3.1. Line profiles and emitting regions

To characterize the line profiles in an observational way we calculate the typical wavelength and widths of the lines. The typical wavelength of the line is calculated as the first wavelength moment of the flux (center of flux) and the typical widths as the blue- and red-side regions containing 76 percent of the flux, corresponding to the half-width-half-maximum (HWHM) of a Gaussian profile. Both these quantities are quite insensitive to the continuum subtraction and are thus suitable for characterization and comparison to other SNe. The continuum level is determined by a linear interpolation between the minimum flux levels

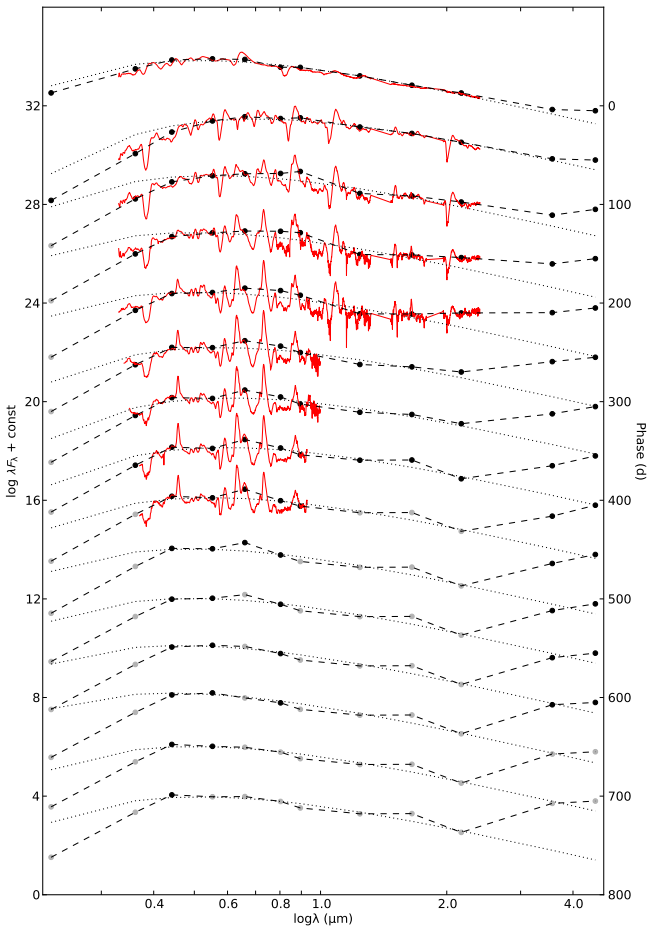

Fig. 8. The evolution of the SED as calculated with the photometric method (black dots and dashed lines) overplotted with blackbody fits to the V, I, J, H and K photometry (black dotted lines) as well as the observed spectra interpolated as described in Sect. 2.3.2 (red solid lines). Fluxes based on extrapolated magnitudes are displayed in shaded colour.

on the blue and red sides within a region set to ±6000 km s^{-1} for most of the lines, ±10000 km s^{-1} for the Ca II 8662 Å line and ±3000 km s^{-1} for the [Fe II] 7155 Å line.

Figure 10 shows the center of flux and blue- and red-side widths as compared to the rest wavelength for the [O I] 6300,6364 Å, [O I] 5577 Å, Mg I] 4571 Å, Na I 5890,5896 Å, [Ca II] 7291,7323 Å, Ca II 8498,8542,8662 Å and [Fe II] 7155 Å lines calculated with this method. The rest wavelength is assumed to be 6316 Å for the [O I] 6300,6364 Å line as is appropriate for a line ratio of 3 and 5993 Å, 7307 Å and 8662 Å for the Na I 5890,5896 Å, [Ca II] 7291,7323 Å and Ca II 8498,8542,8662 Å lines respectively.

To estimate the sizes of the line emitting regions and the absorptive continuum optical depths required to cause the blueshift of the typical wavelength seen in many lines we use a method based partly on the knowledge gained from J14. For lines found to be optically thin using the steady-state NLTE modelling, we fit the line profile of a spherically symmetric region of constant line emissivity, optically thin in the line and with a constant absorptive continuum opacity, to the observed line profile. This gives a rough estimate of the size of the region responsible for the bulk of the line emission.

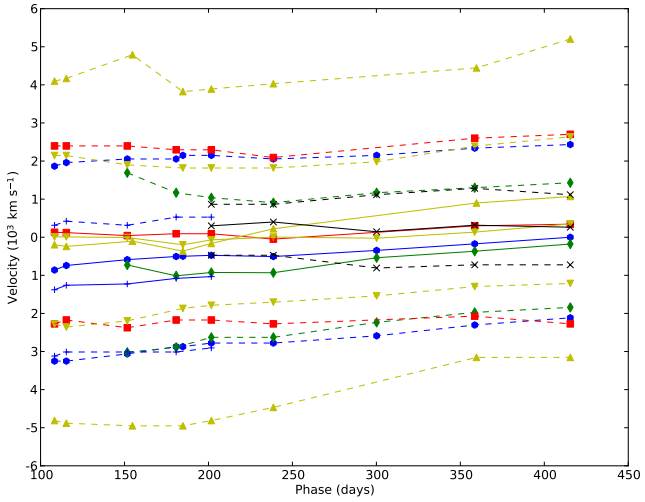

Fig. 10. Center of flux velocities (solid lines) and the blue- and red-side widths (dashed lines) as compared to the rest wavelengths for the [O I] 6300,6364 Å (blue dots), Mg I] 4571] Å (green diamonds), Na I 5890,5896 Å (red squares), [Ca II] 7291,7323 Å (yellow downward triangles), Ca II 8498,8542,8662 Å (yellow upward triangles), [Fe II] 7155 Å (black crosses) and [O I] 5577 Å (blue pluses) lines.

Some lines arise as a blend of more than one line which has to be taken into account. The [O I] 6300 Å flux was calculated by iterative subtraction of the [O I] 6364 Å flux, from the left to the right, using $F_{6300}(\lambda) = F_{6300,6364}(\lambda) - F_{6300}(\lambda - \Delta\lambda)/R$, where $\Delta\lambda$ is the wavelength separation between the [O I] 6300 Å and 6364 Å lines and R the [O I] 6300,6364 Å line ratio. This ratio was assumed to be 3, as is supported by the steady-state NLTE modelling and estimates based on small scale variations (Sect. 3.3.10). In all other cases, where the line ratios of the blended lines are not known, we make a a simultaneous fit assuming the same size of the emitting region for all of the blended lines.

3.3.2. Hydrogen lines

Summary of the findings in J14: No (isolated) hydrogen lines are identified. Some Hα emission arising from the hydrogen-rich envelope is present, but is found to be increasingly dominated by [N II] 6548,6583 Å emission arising from the helium zone after ∼150 days. No detectable absorption is found in Hα or any of the other hydrogen lines.

Figure 9 shows the post 100 days (interpolated) spectral evolution centred on the Hα line. There is a dip in the [O I] 6300,6364 Å line profile after ∼150 days, that corresponds well to the early time Hα absorption minimum at ∼11000 km s^{-1} (E14a). However, as discussed in Sect. 3.3.10, this feature repeats in a number of other lines and is rather due to clumping/asymmetries in the ejecta. There is also an emerging emission feature near the rest wavelength of Hα after ∼200 days which, given the findings in J14, is rather be due to [N II] 6548,6583 Å emission.

Using the method described in Sect. 3.3.1, we find the feature to be well fitted by emission from a region with a radius of 5500 km s^{-1}, emitting mainly in the [N II] 6583 Å line, although the wings of the observed line profile may extend to ∼12000 km s^{-1} on the red side. Hα emission from the hydrogen-rich envelope is expected to result in a flat-topped line profile, at least 11000

km s^{-1} wide (E14a). The size of the line emitting region, as well as the extent of the wings, is instead consistent with emission from the helium zone, in agreement with the results in J14.

!But the peak at late times is exactly at the rest wavelength of Hα. What does this mean?!

3.3.3. Helium lines

Summary of the findings in J14: The (isolated) helium lines identified are the He I 10830 Å and He I 20581 Å lines, although the He I 10830 Å line is found to be blended with the [S I] 10820 Å line. The helium lines arise mainly from the helium zone, but there is also some contribution from helium in the Fe/Co/He zone. Both lines are found to be optically thick, implying a significant contribution from line scattering.

Figure. 9 shows the post 100 days (interpolated) spectral evolution for the identified helium lines. The He I 10830 Å and He I 20581 Å lines emerge at ∼10 and ∼15 days respectively (E14a) and remain until our spectral coverage ends, both in emission and absorption.

Both the He I 10830 Å and He I 20581 Å lines have P-Cygni like profiles, suggesting a significant contribution from scattering, in agreement with the results in J14. Although the unblended He I 20581 Å line has a quite broad peak it is not flat-topped, suggesting a contribution from helium at low velocities. This is again in agreement with the results in J14, where we find helium in the Fe/Co/He zone to contribute significantly at low velocities.

3.3.4. Oxygen lines

Summary of the findings in J14: The (isolated) oxygen lines identified are the [O I] 5577 Å, O I 7774 Å, O I 9263 Å, O I 11300 Å, O I 13164 Å and [O I] 6300,6364 Å lines, although the O I 9263 Å line is found to be blended with the [Co II] 9338,9344 Å line on the red side. All these lines are found to arise from the oxygen zones, the part arising from the O/C and O/Si/S zones depending sensitively on the amount of molecule (CO and SiO) cooling in these zones.

Figure 9 shows the post 100 days (interpolated) spectral evolution for the identified oxygen lines. The allowed oxygen lines emerge between ∼25 and ∼50 days (E14a) and, except for the [O I] 5577 Å line which disappears at ∼300 days, remain until our spectral coverage ends. The [O I] 6300,6364 Å line emerge at ∼100 days and remains until our spectral coverage ends.

We measure the radius of the [O I] 6300,6364 Å line emitting region to 3400, 3100 and 2900 km s^{-1} at 202, 300 and 415 days respectively. The line profile fits (Fig.11) are quite good, but the observed emission is underestimated at low velocities and extends to at least ∼5000 km s^{-1}, suggesting radially decreasing emissivity.

The center of flux of the [O I] 6300,6364 Å line shows a blue-shift of ∼1000 km s^{-1} at 100 days, decreasing towards zero at 400 days, whereas the center of flux of the [O I] 5577 Å line shows a blue-shift of ∼1500 km s^{-1} at 100 days, decreasing towards ∼1000 km s^{-1} at 200 days, when the line begins to fade away. We do not find any significant blue-shifts of the O I 11300 and 13164 Å lines. The blue-shifts are discussed further in Sect.3.3.11, where we compare to observation of other SNe, and in J14, where we suggest the physical cause to be line-blocking in the core.

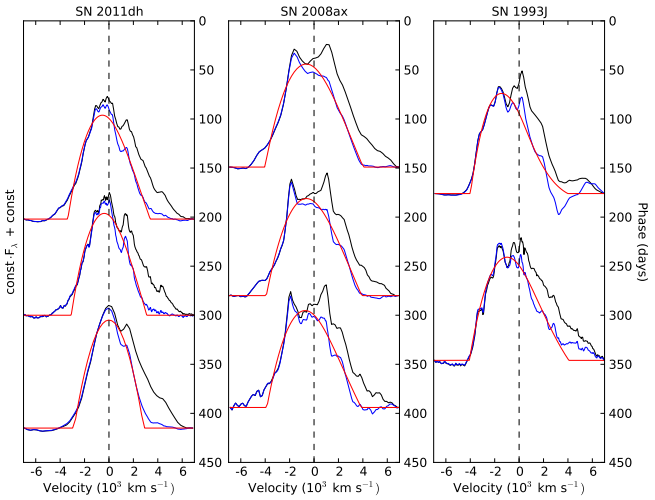

Fig. 11. [O I] 6300,6364 Å (black) and decomposed [O I] 6300 Å (blue) line profiles at selected epochs as compared to line profile fits (red) for SNe 2011dh (left panel), 2008ax (middle panel) and 1993J (right panel).

3.3.5. Sodium lines

Summary of the findings in J14: The only (isolated) sodium line identified is the Na I 5890,5896 Å line. Observationally this line is hard to disentangle from the He I 5876 Å line, but the emission is found to arise mainly from the Na I 5890,5896 Å line (although absorption could be a blend), and to be a combination of recombination emission from the O/Ne/Mg zone and scattering throughout the ejecta.

Figure 9 shows the post 100 days (interpolated) spectral evolution for the Na I 5890,5896 Å line. The line has a P-Cygni like profile, suggesting a significant contribution from scattering, in agreement with the results from J14 and remains, both in emission and absorption, until our spectral coverage ends.

3.3.6. Magnesium lines

Summary of findings in J14: The (isolated) magnesium lines identified are the Mg I] 4571 Å and Mg I 15040 Å lines, and both are found to arise mainly from the O/Ne/Mg zone.

Figure 9 shows the post 100 days (interpolated) spectral evolution for the identified magnesium lines. The Mg I] 4571 Å line emerges at ∼150 days whereas the Mg I 15040 Å line may emerge as early as ∼40 days (E14a) and both remain until our spectral coverage ends.

We measure the radius of the Mg I] 4571 Å line emitting region to 3600, 2800 and 2700 km s^{-1} at 202, 300 and 415 days respectively, and the radius of the Mg I 15040 Å line emitting region to 3400 and 2900 km s^{-1} at 89 and 205 days respectively. The line profile fits (Fig. 12) of the Mg I] 4571 Å line are quite good, but the observed emission is underestimated at low velocities and extends to at least ∼5000 km s^{-1}, suggesting radially decreasing emissivity.

The center of flux of the Mg I] 4571 Å line shows a blue-shift of ∼1000 km s^{-1} at ∼200 days, decreasing towards a few hundred km s^{-1} at ∼400 days. We do not find any significant blue-shift of the Mg I 15040 Å line. The blue-shifts are discussed further in Sect.3.3.11, where we compare to observation of other

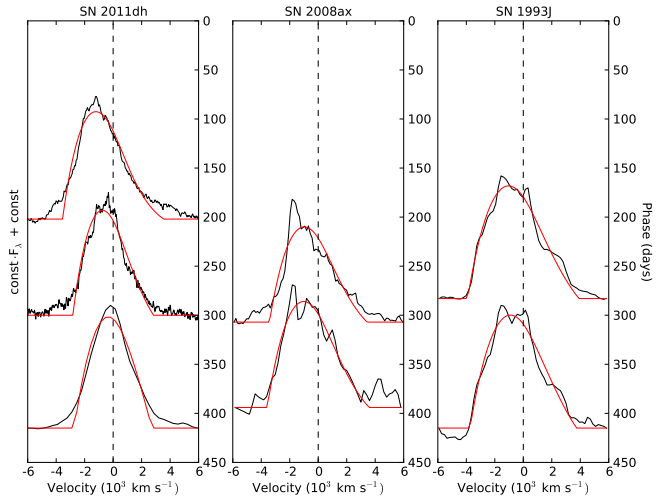

Fig. 12. Mg I] 4571 Å line profiles (black) at selected epochs as compared to line profile fits (red) for SNe 2011dh (left panel), 2008ax (middle panel) and 1993J (right panel).

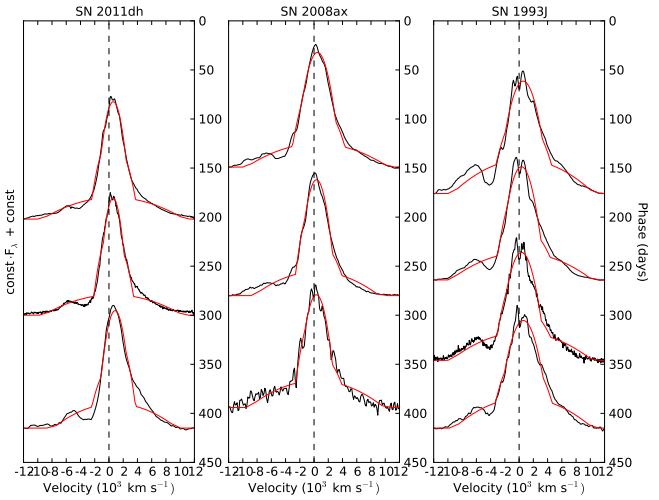

Fig. 13. [Ca II] 7291,7323 Å line profiles (black) at selected epochs as compared to line profile fits (red) for SNe 2011dh (left panel), 2008ax (middle panel) and 1993J (right panel).

SNe, and in J14, where we suggest the physical cause to be line-blocking in the core.

The estimated radius of the Mg I line emitting region of 2700-3600 km s^{-1} is similar to the estimated radius of the O I line emitting region of 2900-3400 km s^{-1}. As mentioned above the Mg I lines are found in J14 to arise from the O/Ne/Mg zone and the O I lines to arise from the O/Ne/Mg zone and, depending on the amount of molecule (CO and SiO) cooling, the O/C and O/Si/S zones. As is evident from Figs. 11 and 12 (but see also Fig. 16) the profiles of the [O I] 6300 and the Mg I] 4571 Å lines are very similar, suggesting these to arise from the O/Ne/Mg zone. In Sect. 3.3.10 we find this to be true also for small scale variations in the line profiles in further support of this hypothesis.

3.3.7. Calcium lines

Summary of the findings in J14: The (isolated) calcium lines identified are the Ca II 3934,3968 Å, Ca II 8498,8542,8662 Å and [Ca II] 7291,7323 Å lines. Absorption in the Ca II 3934,3968 Å lines is found to occur throughout the ejecta and the Ca II 8498,8542,8662 Å lines to arise mainly from fluorescence in these lines. The [Ca II] 7291,7323 Å lines, on the other hand, is found to arise mainly from the Si/S zone, with a possible contribution throughout the ejecta from fluorescence in the Ca II 3934,3968 Å lines. The Ca II 8498,8542,8662 Å line is found to be blended with the [C I] 8727 Å line, arising mainly from the O/C zone, the amount of blending depending sensitively on the amount of molecule (CO) cooling in this zone.

Figure 9 shows the post 100 days (interpolated) spectral evolution for the identified calcium lines. The Ca II 3934,3968 Å line is present initially in absorption (E14a) and remains so until the spectral coverage ends. The Ca II 8498,8542,8662 Å line is present initially with a P-Cygni profile (E14a), but disappears in absorption at ∼100 days. The Ca II 8498,8542 Å lines disappear in emission at ∼300 days, whereas the Ca II 8662 Å line remains until the spectral coverage ends. The [Ca II] 7291,7323 Å line emerges at ∼100 days and remains until the spectral coverage ends.

We measure the radii of a two-component [Ca II] 7291,7323 Å line emitting region to 2400/9900, 2100/9100 and 2400/9000 km s^{-1} at 202, 300 and 415 days respectively. The line profile fits (Fig. 13) are good in the inner region but worse in the wings, which are quite asymmetric and also blended with the [Fe II] 7155 Å line on the blue side. The more pronounced red-side wing could indicate a P-Cygni like contribution from scattering.

The center of flux for the Ca II 8498,8542,8662 Å line shows a red-shift increasing towards ∼1000 km s^{-1} at 400 days. As the center of flux is calculated with respect to the rest wavelength of the Ca II 8662 Å line (Sect. 3.3.1) this suggests a significant contribution from the [C I] 8727 Å line to the flux, which is in agreement with the results from J14 if the amount of molecule (CO) cooling in the C/O zone is modest.

The size of the inner [Ca II] 7291,7323 Å line-emitting region of 2100-2400 km s^{-1} is less than the 2700-3600 km s^{-1} found for the Mg I and O I line emitting regions which, assuming this emission arises mainly from the Si/S zone (see above), suggests partial mixing of the Si/S zone and the surrounding oxygen zones. The size of the outer [Ca II] 7291,7323 line-emitting region of 9000-9900 km s^{-1} implies a contribution from calcium in the helium zone.

3.3.8. Iron group lines

Summary of the findings in J14: The (isolated) iron lines identified are the [Fe II] 7155 Å, [Fe II] 12600 Å and [Fe II] 16400 Å lines. The (isolated) cobalt lines identified are the [Co II] 9338,9344 Å, [Co II] 10190,10248,10283 Å and [Co II] 15475 Å lines, although the [Co II] 9338,9344 Å line is found to be blended with the O I 9263 Å line on the blue side. All of the identified iron and cobalt lines are found to arise from the Fe/Co/He zone.

Figure 9 shows the post 100 days (interpolated) spectral evolution for the identified iron and cobalt lines. The [Fe II] 7155 Å line emerges at ∼150 days and remains until our spectral coverage ends. The [Fe II] 12600 Å and [Fe II] 16400 Å lines are identified in our last NIR spectrum at ∼200 days, although the identification of the former is a bit doubtful given the large offset from the rest wavelength. The [Co II] 9338,9344 Å line may

emerge as early as ∼50 days and remains until our spectral coverage ends, whereas the [Co II] 10190,10248,10283 Å and [Co II] 15475 Å lines are identified in our last NIR spectrum at ∼200 days.

We measure the radius of the [Fe II] 7155 Å line emitting region to 1600 km s^{-1} at 300 and 415 days, and the radius of the [Fe II] 16440 Å line emitting region to 2100 km^{-1} at 206 days. We also measure the radius of the [Co II] 10190,10248,10283 Å line emitting region to 2000 km s^{-1} at 206 days. The [Co II] 15475 Å line is noisy, but we find the radius of the line-emitting region to be 3200 km s^{-1} at 206 days. As mentioned the [Co II] 9338,9344 Å line is blended with the O I 9263 Å line on the blue side, and also appears to be blended with other lines on the red side, so we do not attempt to estimate the radius of the line emitting region.

Except for the [Co II] 15475 Å line at 206 days, the estimates of the size of the Fe II and Co II line emitting region lie in the range 1600-2100 km s^{-1}, significantly smaller than the 2700-3600 km s^{-1} estimated for the O I and Mg I line emitting region. This is consistent with a scenario where the Fe/Co/He core and the surrounding oxygen zones are only partially mixed. However, as discussed in Sect. 4.5, hydrodynamical modelling of the early lightcurve strongly suggests that some amount of Fe/Co/He core material has been mixed far out in the ejecta. This is not neccesarily in conflict with the Fe II and Co II line profiles as this amount may be small enough not to be clearly visible.

3.3.9. CO overtone band

Figure 14 shows continuum subtracted observed *K* band spectra at 89 and 206 days compared to the synthetic *K* band spectrum at 200 days for the optimal steady-state NLTE model (Sect. 4.1). The region where we expect CO overtone emission is marked in the figure and is assumed to be 22750-24350 Å (reference). The continuum was estimated as a linear interpolation between the endpoint fluxes of the region averaged over 100 Å. As seen in Fig. 14 there is a clear excess in the region both compared to the continuum and the model spectrum and the shape and extent of the feature is similar at 89 and 202 days. Although other explanations cannot be excluded we find it reasonable to interpret this feature as CO overtone emission.

The integrated continuum subtracted flux in the region was 3.1×10^{-14} and 8.1×10^{-15} erg s^{-1} cm^{-2} at 89 and 206 days respectively. These values should be taken with some caution as they depend sensitively on the method used to subtract the continuum. The total flux in the 4.5 μm band, which contains the region where we expect CO fundamental band emission, calculated using the zeropoint flux and the equivalent width of the band, was 4.9×10^{-13} and 1.7×10^{-13} erg s^{-1} cm^{-2} at 89 and 206 days respectively. Note that the value at 206 days lies in the gap of the Spitzer observations and has been linearly interpolated between 85 and 251 days. If all of the flux in the 4.5 μm band was due to CO fundamental band emission this would correspond to fundamental to overtone band flux ratios of ∼15 and ∼20 at 85 and 206 days respectively.

3.3.10. Small scale fluctuations

Figure 15 shows small scale fluctuations in the [O I] 6300,6364 Å, [O I] 5577 Å, O I 7774 Å, Mg I] 4571 Å and Na I 5890,5896 Å lines at 202 and 300 days. The resolution is ∼600 and ∼250 km s^{-1} in the 202 and 300 days spectra respectively. A 1000

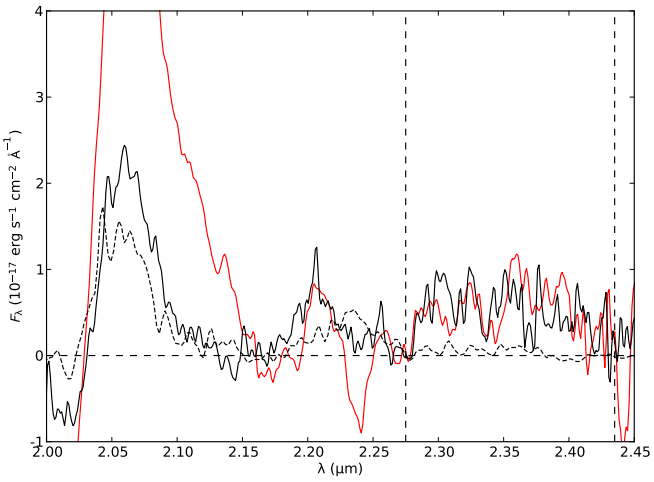

Fig. 14. Continuum subtracted observed *K* band spectra at 89 (red solid line) and 206 (black solid line) days compared to the continuum subtracted synthetic *K* band spectrum at 200 days (black dashed line) for the optimal steady-state NLTE model. The CO overtone region have been marked by black dashed lines and the observed flux at 206 days scaled with the ratio of the measured total CO overtone fluxes.

km s^{-1} box average of the line profile was repeatedly (3 times) subtracted to enhance the small scale fluctuations. We have tested this method on the product of synthetic large and small scale structures and the small scale structure is recovered with reasonable accuracy. In the upper left panel we show a comparison of the [O I] 6300 Å line profiles at 202 and 300 days. These are very similar and there is not much evolution of the small scale fluctuations in the line profile during this period. We identify 8 features marked A-H with an FWHM between 300 and 600 km s^{-1} present at both epochs.

However, features G and H interpreted as belonging to the [O I] 6364 Å line match very well with the E and F features interpreted as belonging to the [O I] 6300 Å line so these are likely to be repetitions. Minimizing the RMS (Root Mean Square) of the small scale fluctuations redwards 3000 km s^{-1} (G and H), where the [O I] 6364 Å flux was subtracted from the [O I] 6300,6364 Å line profile using the method described in Sect. 3.3.1, we find a line ratio of 2.9 at 202 and 300 days to give a complete removal of features G and H. This ratio is in agreement with the value of 3 expected for optically thin emission and also with the results from J14.

In the upper right panel we show the corrected [O I] 6300 Å line profile and in the lower left panel we show a comparison to the Mg I] 4571 Å line profile at 300 days. All features except B are clearly identified and the agreement is good. The features on the red side are weaker for the Mg I] 4571 Å line, which is consistent with the larger red-side flux deficit for this line, but the relative (flux normalized) strength of all features are similar. The good agreement suggests that the [O I] 6300 Å and Mg I] 4571 Å lines arise from the same nuclear burning zones. Given that the Mg I] 4571 Å line arises mainly from the O/Ne/Mg zone, as found in J14, it also suggests that the [O I] 6300 Å line arises mainly from this zone and that the contribution from the O/Si/S and O/C zones are modest.

In the lower right panel we show a comparison of the corrected [O I] 6300 Å line profile and the [O I] 5577 Å, O I 7774 Å and Na I 5890,5896 Å line profiles at 202 days. The E and F features are clearly identified in all of these line profiles, but

none of the other features are seen. Since the E and F features are also the strongest it is not clear if the absence of the other features is real or if the other features are just too faint to be seen. The relative strength of the E and F features are similar for the [O I] 5577 Å, O I 7774 Å and [O I] 6300 Å lines, suggesting that all these lines arise mainly from the same nuclear burning zones, whereas the relative strength of these features for the Na I 5890,5896 Å line is a bit (∼50 percent) weaker, suggesting contributions from other nuclear burning zones. This is in agreement with the results in J14, where all oxygen lines are found to arise from the oxygen zones and the Na I 5890,5896 Å line partly from the O/Ne/Mg zone.

The small scale fluctuations in the [Ca II] 7291,7323 Å line (not shown) do not match very well with those in the [O I] 6300 Å line and the relative strength of the features seen is weaker. We were not able to correct for blending as for the [O I] 6300,6364 Å line, which makes the interpretation less clear, but the result is in agreement with the results in J14, were we found this line to arise from other nucluear burning zones. This is also suggested by the different sizes of the line emitting regions discussed in Sect. 3.3.7.

Shivvers et al. (2013) presented an analysis of the line profiles of the [O I] 6300,6364 Å, O I 7774 Å and Mg I 4571 Å lines at 268 days. By decomposition of the [O I] 6300,6364 Å line profile into Gaussian profiles, assuming an [O I] 6300,6364 Å line ratio of 3, they found a good fit for one broad and two narrow profiles located at -400 and 1600 km s^{-1}. The two strongest features in our analysis, E and F, are located at ∼0 and ∼1500 km s^{-1} and likely correspond to the two features found by Shivvers et al. (2013). They also find these features to repeat in the O I 7774 Å and Mg I 4571 Å lines, in agreement with our analysis. The difference in velocity for the E feature is likely explained by the different methods used.

Matheson et al. (2000) presented an analysis of the small scale fluctuations in the line profiles of SN 1993J. They found a good agreement between the fluctuations in the [O I] 6300 Å, [O I] 5577 Å and O I 7774 Å line profiles, which is in agreement with our results for SN 2011dh. However, they did not find a good agreement between the fluctuations in the [O I] 6300 Å and Mg I] 4571 Å line profiles, which is a bit surprising since we find an excellent agreement between fluctuations in these lines for SN 2011dh. One possible explanation is that the [O I] 6300 Å line is dominated by flux from the O/Ne/Mg zone for SN 2011dh but not for SN 1993J, as we expect the Mg I] 4571 Å line to emerge from this zone, whereas the oxygen lines could also have contributions from the O/Si/S and O/C zones.

The small scale fluctuations observed provide evidence for a clumpy ejecta as previously demonstrated for SNe 1993J (Matheson et al. 2000) and 1987A (Stathakis et al. 1991; Chugai 1994). In a simplified way we may represent the material of some nuclear burning zone by a number of randomly distributed clumps, having a typical size and occupying some fraction of the ejecta volume (filling factor). The small scale fluctuations in the line profiles then arise from statistical fluctuations in the distribution of the clumps, the RMS of the fluctuations increasing with decreasing number of clumps and/or filling factor and/or increasing size of the clumps. In J14 we use the statistical model by Chugai (1994) to calculate an upper limit on the filling factor of ∼0.07 for oxygen zone material within the sphere containing the bulk of this material, in agreement with the value of ∼0.06 estimated for SN 1993J by Matheson et al. (2000) using the same method.

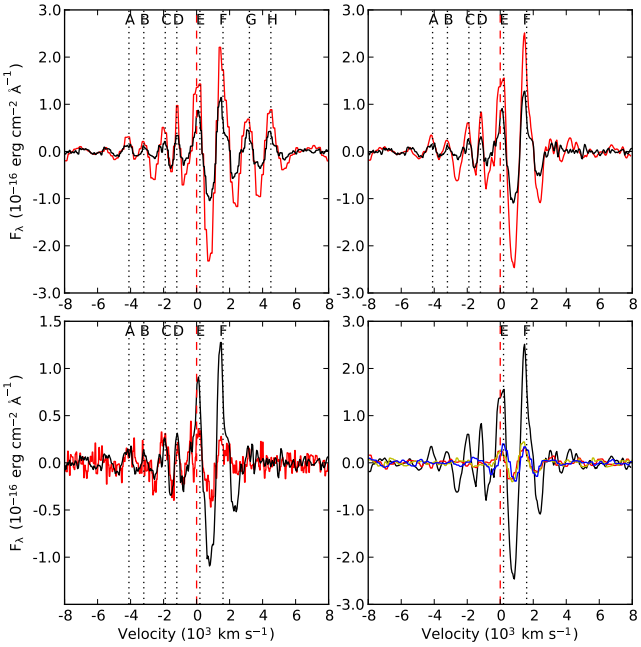

Fig. 15. Comparison of box average subtracted line profiles. The upper left panel shows the [O I] 6300 Å line profile at 202 (red) and 300 (black) days. The upper right panel shows the corrected [O I] 6300 Å line profile at 202 (red) and 300 (black) days. The lower left panel shows the corrected [O I] 6300 Å line profile (black) and the Mg I] 4571 Å line profile (red) at 300 days. The lower right panel shows the corrected [O I] 6300 Å line profile (black) and the [O I] 5577 Å (red), O I 7774 Å (green) and Na I 5890/5896 Å (blue) line profiles at 202 days.

3.3.11. Comparison to SNe 1993J and 2008ax

Figures 11, 12 and 13 show a comparison of the (continuum subtracted) [O I] 6300 Å, Mg I] 4571 Å and [Ca II] 7291,7323 Å line profiles and fits using the method described in Sect. 3.3.1 for SNe 2011dh, 2008ax and 1993J respectively. The estimated radii of the line emitting regions are 4000-4100 and 3900-4000 km s^{-1} for the [O I] 6300 Å line, 3700-3900 and 3400-3600 km s^{-1} for the Mg I] 4571 Å line and 3000-3400 and 2600-3000 km s^{-1} for the [Ca II] 7291,7323 Å line for SNe 1993J and 2008ax respectively. These radii are in all cases significantly larger than the radii of the line emitting regions estimated for SN 2011dh (Sect. 3.3.4, 3.3.6 and 3.3.7), and are in all cases larger for SN 1993J than for SN 2008ax. The radius of the [Ca II] 7291,7323 Å line emitting region is in all cases smaller than the radii of the [O I 6300] Å and Mg I] 4571 Å line emitting regions, suggesting partial mixing of the Si/S zone and the surrounding oxygen zones as previously discussed for SN 2011dh in Sect. 3.3.7.

The shapes of the [O I] 6300 Å and Mg I] 4571 Å line profiles for SNe 2008ax and 1993J differer from those of SN 2011dh and are significantly flatter at low velocities, most pronounced for SN 2008ax. This would in a spherically symmetric geometry suggest a lower fractional emissivity at low velocities as compared to SN 2011dh and possibly a decreasing emissivity or even a void at low velocities. The shape of the [Ca II] 7291,7323 Å line profiles on the other hand are similar and centrally peaked for all SNe. Note that the double peaks of the [O I] 6300,6364 Å line profile for SN 2008ax discussed by Taubenberger et al. (2011), Maurer et al. (2010) and Milisavljevic et al. (2010) seem to be well explained by a repetition of the blue peak in the [O I] 6364

Å line and that this blue peak also seem to repeat in the Mg I] 4571 Å line.

Figure 16 shows the continuum subtracted mirrored blue-side profiles for the [O I] 6300 Å, Mg I] 4571 Å, [Ca II] 7291 Å and [Fe I] 7155 Å lines for SNe 2011dh, 2008ax and 1993J at 300, 307 and 283 days respectively. This figure nicely illustrates the different sizes of the line emitting regions and shapes of the line profiles discussed above. The blue side is less affected by obscuration as compared to the red side and contamination from the [O I] 6364 Å and [Ca II] 7323 Å lines to the [O I] 6300 Å and [Ca II] 7291 Å lines is probably modest, although the [Ca II] 7291,7323 Å line ratio is uncertain. Note the remarkable similarity between the [O I] 6300 Å and Mg I] 4571 Å line profiles seen for all SNe, previously discussed for SN 2011dh in Sect. 3.3.6 and 3.3.10.

For SN 2008ax a number of lines, including the Na I 5890,5896 Å, [O I] 5577 Å, O I 7774 Å, Mg I 15040 Å, He I 10830 Å and He I 20581 Å lines, show flat-topped profiles either on the blue or both sides similar to those of the [O I] 6300 Å and Mg I] 4571 Å lines. This behaviour is quite different from SN 2011dh where no lines, except possibly the He I 20581 Å line, show flat-topped profiles. It is tempting to speculate that the differences in the shapes of line profiles, as well as the sizes of the line emitting regions, among the SNe are related to the geometry of the ejecta (or part of it) and differences in the viewing angle. In Sect. 4.5 we show that the explosion energy as well as the ejecta mass as determined from hydrodynamical modelling is similar for the three SNe (although the error bars are large). Assuming the geometry is similar for all three SNe we would observe broader and more flat-topped line-profiles if the ejecta is either elongated along the line-of-sight (e.g. bi-polar) or compressed along an axis perpendicular to the line-of-sight (e.g. disc or torus). However, more flat-topped line profiles would also be a natural consequence of a smaller degree of macroscopic mixing, preserving more of the original onion-like structure of the ejecta.

Figure 17 shows the center of flux velocities for the [O I] 6300,6364 Å, [O I] 5577 Å, Mg I] 4571 Å and [Ca II] 7291,7323 Å lines calculated as described in Sect. 3.3.1 for SNe 2011dh, 2008ax and 1993J. As discussed in Sects. 3.3.4 and 3.3.6 there is a blue-shift of the [O I] 6300,6364 Å, [O I] 5577 Å and Mg I] 4571 Å lines for SN 2011dh which, as seen in Fig. 17, is also present, and even more pronounced for SNe 2008ax and 1993J. For SN 2011dh this blue-shift disappears towards 400 days but for SNe 2008ax and 1993J the blue-shift saturates at ~500 km s^{-1} after 200 days. In J14 we provide a thorough discussion of these blue-shifts and suggest the cause to be line-blocking in the core based on results from the steady-state NLTE modelling. There is no significant blue shift in the O I 11300 Å, O I 13164 Å and [Mg I] 15040 Å lines for SNe 2011dh (Sects. 3.3.4 and 3.3.6) and 2008ax in support of this hypothesis, as line-blocking is less effective in the NIR (J14). Milisavljevic et al. (2010) find the [O I] 6300,6364 Å, [O I] 5577 Å and Mg I] 4571 Å lines to be either symmetric or asymmetric towards the blue for a sample of 18 stripped envelope SNe whereas Taubenberger et al. (2009) find a systematic blue-shift of the [O I] 6300,6364 Å line disappearing with time for another, partly overlapping, sample of 39 stripped envelope SNe. Both these results favours obscuration of the receding-side emission and disfavours ejecta assymetries as the explanation, whereas the latter result is in agreement with our results for SN 2011dh and disfavours obscuration by dust. However, to explain the saturation of the blue-shifts for SNe 2008ax and 1993J the evolution of the core-opacity needs to be different for these SNe as compared to SN 2011dh. It is worth noting that a higher optical depth in the core for SNe 2008ax and 1993J would be a natural consequence of the viewing angle for the ejecta geometries discussed above.

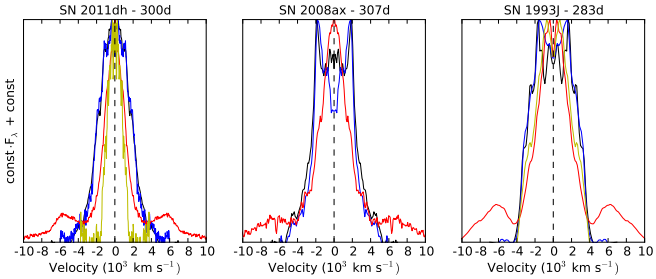

Fig. 16. Continuum subtracted mirrored blue-side profiles for the [O I] 6300,6364 Å (black), Mg I] 4571 Å (blue), [Ca II] 7291,7323 Å (red) and [Fe I] 7155 Å (yellow) lines for SNe 2011dh, 2008ax and 1993J at 300, 307 and 283 days respectively.

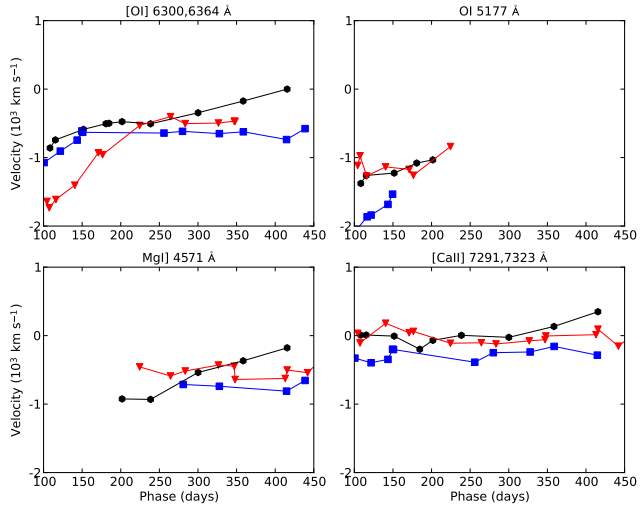

Fig. 17. Center of flux velocities for the [O I] 6300,6364 Å (upper left panel), [O I] 5577 Å (upper right panel) Mg I] 4571 Å (lower left panel), [Ca II] 7291,7323 Å (lower right panel) lines for SNe 2011dh (black dots), 2008ax (blue squares) and 1993J (red triangles).

4. Modelling

In this section we discuss modelling of the bolometric and photometric lightcurves with the steady-state NLTE code described in Jerkstrand et al. (2011, 2012) and J14 and HYDE, a hydrodynamical code described in E14b. Given the extensive coverage for SN 2011dh, both in time and wavelength, consistent modelling of the bolometric and photometric lightcurves throughout the evolution is highly desirable. Ideally, HYDE would be used to evolve a grid of initial stellar models through a parametrized explosion and the photospheric phase and the resulting ejecta models then fed into the steady-state NLTE code and subsequently evolved. The resulting grid of SN models, spanning the progenitor and SN parameter space, could then be fitted to observations and the degeneracy of the solution and the errors in the parameters quantified. For the 0-100 days evolution we have used the grid of SN models, constructed with HYDE and MESA STAR, presented in E14b, but to evolve this 15×10×9×9

grid further with the steady-state NLTE code is not computationally feasible. We are thefore forced to use the hydrodynamical grid for the early evolution (0-100 days) and a highly restricted set of steady-state NLTE models, presented in J14, for the late evolution (100-500 days). Furthermore, these steady-state NLTE models are artificially constructed and have not been evolved through the 0-100 days period with a hydrodynamical code. To partly circumvent these problems we try two different approaches. First, to extend the temperal coverare of the J14 models to early times we evolve these through the 0-100 days period using HYDE in homologous mode. Secondly, to extend the temporal coverage of the hydrodynamical model grid to 300 days we apply a correction for the flux within the observed wavelength determined with the steady-state NLTE code. The optimal steady-state NLTE model, presented in J14, is chosen to give the best agreement with both nebular spectra and the bolometric and photometric lightcurves. In J14 we discuss the constraints on the model parameters from nebular spectra and in this paper we discuss the constraints on the model parameters obtained from the bolometric and photometric lightcurves. Finally, as discussed in Sect. 4.4, after ∼500 days time-dependent effects becomes important and a steady-state assumption is no longer valid. Therefore the steady-state NLTE models are restricted to the 100-500 days period.

Except for the covered volyme of parameter space there is important differences between the hydrodynamical and the steady-state NLTE modelling. As HYDE assumes spherical symmetry, the macrosopic mixing of the ejecta arising from hydrodynamical instabilities in multidimensional simulations is prohibited. The steady-state NLTE code on the other hand is capable of handling a macroscopically mixed ejecta in a statistical sense, although the overall structure is assumed to be spherical symmetric. As HYDE is based on the diffusion approximation and grey opacities it is only suitable for bolometric lightcurves. The steady-state NLTE code on the other hand, which solves the statistical equilibrium equations and the frequency dependent radiative transfer, is capable of producing photometric and pseudo-bolometric lightcurves. As the steady-state NLTE code does not have hydrodynamical capabilities, requires steady-state and experiences other difficulties when the optical depths are high it can not be used at times earlier than ∼100 days. HYDE, on the other hand, has the hydrodynamical and time-dependent capabilities needed to evolve the SN through the explosion and the diffusion phase. On the tail, where the diffusion time is short and steady-state is satisfied, both codes has the capability to produce bolometric lightcurves and in fact use the same radiative transfer model to calculate the deposition of the radioactive decay energy. So in this phase the advantage of the steady-state NLTE code is the capability to calculate pseudo-bolometric and photometric lightcurves covering the observed wavelength regions.

The outline of the section is as follows. In Sect. 4.1 we discuss modelling of the 100-500 days bolometric and photometric lightcurves with the steady-state NLTE code using the J14 ejecta models and in Sect. 4.2, 4.3 we discuss the effects on these lightcurves by dust absorption and emission and molecule emission. In Sect. 4.4 we discuss the 500-750 days bolometric lightcurves and the effects of time dependent processes and other additional energy sources in this phase. In Sect. 4.5 we fit the 0-100 days bolometric lightcurves of SNe 2011dh, 1993J and 2008ax to the grid of SN models grid constructed with HYDE and MESA STAR presented in Ergon et al. (2014a). In Sect. 4.6 we extend the temporal coverage of this model grid to 300 days by the use of a correction for the flux within the observed wavelength range determined by the steady-state NLTE modelling and apply this to the observed 0-300 days bolometric lightcurve of SN 2011dh.

4.1. NLTE modelling of the 100-500 days bolometric lightcurve

In this section we compare synthetic pseudo-bolometric and photometric lightcurves for the J14 steady-state NLTE models to the observed 100-500 days pseudo-bolometric and photometric lightcurves. Contrary to the hydrodynamical model grid used in Sects. 4.5 and 4.6, these models spans only a restricted volume of parameter space and the degeneracy of the solution and the errors in the results can not be quantified. The optimal model, presented in J14, have been chosen to give the best agreement with both nebular spectra and the bolometric and photometric lightcurves. In J14 we discuss the contraints on the model parameters provided by the nebular spectra and here we discuss the constraints provided by the bolometric and photometric lightcurves. The set of models, listed in table 2 in J14, varies in at least one of the following parameters, initial mass (12, 13 or 17 $M_\odot$), degree of macroscopic mixing (medium or strong), positron trapping (local or free-streaming), molecule cooling (yes or no), dust absorption/emission (yes or no) and oxygen zone filling factor (small-large). The optimal model (12C) has an initial mass of 12 $M_\odot$, strong macroscopic mixing, local positron trapping, no molecule cooling, dust absorption/emission and an oxygen zone filling factor of 0.043. The meaning of each parameter and the different configurations used are described in detail in J14.

The underlying 12, 13 and 17 $M_\odot$ ejecta models are constructed using abundancies from Woosley & Heger (2007) and density profiles for the helium and hydrogen envelopes from B12, and are described in detail in J14. The sizes of the core (Fe/Co/He to O/C), the helium and hydrogen envelopes has been fixed from constraints derived for SNe 2011dh, 2008ax and 1993J in this and other works. This provides a rough constraint on the quantity E/M and corresponds to the fitting of photospheric velocities in the hydrodynamical modeling in Sects. 4.5 and 4.6. The mass of ejected ^{56}Ni has been set 0.075 $M_\odot$ for all models as determined by hydrodynamical modelling in B12 and this paper. As the J14 models have been artificially constructed and have not been evolved through the 0-100 days evolution, we use HYDE in homologous mode to produce bolometric lightcurves for this phase and compare to the observed U to 4.5 μm pseudo-bolometric lightcurve. The initial temperature profile is taken to be that of the optimal (extended) hydrodynamical model found in Sect. 4.5. In the optimal (extended) hydrodynamical model homology is reached, and the thermal explosion energy gets exhausted, at ∼3 days, so these assumptions are not critical for the subsequent evolution.

Figure 18 shows the 100-500 days U to 4.5 μm, U to K and U to z optimal model (12C) and observed pseudo-bolometric lightcurves. The optimal model U to z pseudo-bolometric lightcurve, for which we have full observational coverage, shows a good agreement with observations and the differences are at the ∼10 percent level. The optimal model U to K and U to 4.5 μm pseudo-bolometric lightcurves shows a similar good agreement until ∼300 days, where our NIR coverage ends, and then the differencies slowly increase to ∼50 and ∼20 percent for the U to K and U to 4.5 μm pseudo-bolometric lightcurves, respectively. Given the uncertainty in the extrapolations of the NIR photometry, which would affect the U to K pseudo-bolometric lightcurve most, these differencies are not too worrying. Fig. 19 shows the 0-100 days bolometric lightcurves for the J14 models

calculated with HYDE compared to the observed U to 4.5 μm pseudo-bolometric lightcurve. The bolometric lightcurve for the optimal model shows an good overall agreement, although the peak is overproduced by ~20 percent. Finally, Fig. 20 shows the U to 4.5 μm lighcurves for the J14 models compared to the observed lightcurves. The lightcurves of the optimal model show an overall agreement with observations but there are some notable exceptions, in particular the 4.5 μm band which we will discuss further in Sect. 4.3.

The pseudo-bolometric luminositiy consists of the product of the bolometric luminosity, depending only on the deposition of radioactive decay energy and the fractional luminosity within the wavelenth range, depending on how this energy is processed. In terms of bolometric corrections we may write $L = L_{\rm Bol}10^{0.4BC}$. As mentioned, the first factor could as well be calculated with HYDE, and it is the ability to determine the second factor that is the strength of the steady-state NLTE code. The split of the pseudo-bolometric lightcurves in two factors that depend in different ways on the model parameters is also very useful for the analysis. Fig. 21 shows the 100-500 days bolometric lightcurves, calculated with HYDE, and the U to 4.5 μm, U to K and U to z bolometric corrections for the J14 models. The bolometric lightcurves (lower panel) depends only on the energy deposition and are therefore independent of molecule cooling and dust emission/absorption, which only affects the processing of the deposited energy. As we discuss below, the filling factors and the positron trapping have negligible effect on the energy deposition for the J14 models as well. Therefore the bolometric lightcurves depends only on the intial mass and the degree of macrospcopic mixing, whereas the bolometric corrections may depend on all model parameters. The U to 4.5 μm bolometric corrections (upper panel) show very small differences (~0.05 mag) during the 100-300 days period, but these subsequently increase towards ~0.5 mag at 500 days. The U to K and U to z bolometric corrections (middle panels), on the other hand, show much larger differences, mainly because molecule cooling and dust absorption/emission affects the distribution of the flux between these wavelength ranges and the MIR. Below we discuss the effects of the initial mass, degree of macroscopic mixing, oxygen zone filling factor and positron trapping on the lightcurves and the constraints these provide on our choice of optimal model. Molecule cooling and dust absorption/emission, are discussed in Sects. 4.3 and 4.2 respectively.

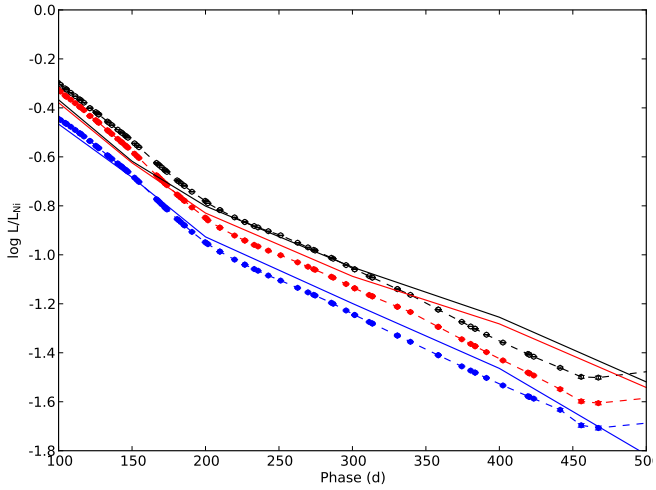

Fig. 18. 100-500 days U to 4.5 μm (black lines), U to K (red lines) and U to z (blue lines) bolometric lightcurves for the optimal model (12C) as compared to the observed U to 4.5 μm (black circles), U to K (red circles) and U to z (blue circles) bolometric lightcurves. The lightcurves have been normalized to the radioactive decay chain luminosity of 0.075 $M_\odot$ of ^{56}Ni.

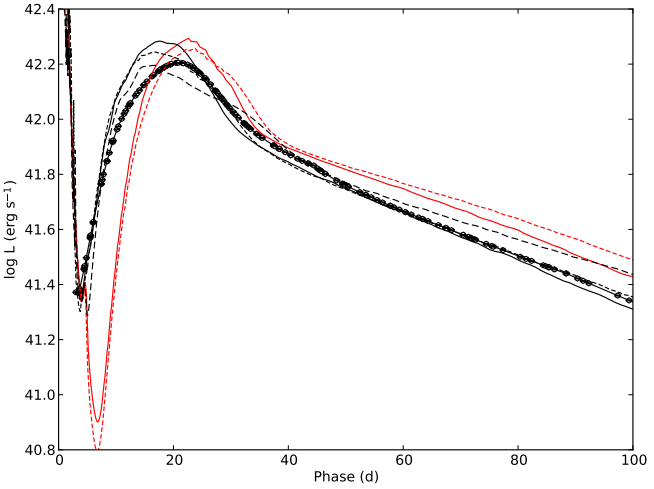

Fig. 19. 0-100 days bolometric lightcurves for the J14 models calculated with HYDE as compared to the observed U to 4.5 μm bolometric lightcurve for the first 100 days. The models are displayed as in Fig. 21.

4.1.1. Initial mass

The initial mass may affect both the energy deposition (bolometric lightcurve) and the way this energy is processed (bolometric correction). Comparing the bolometric lightcurves and bolometric corrections for the optimal model (12C) and models 13G and 17A, which differs only in the intial mass, we find that the effect on the bolometric lightcurve, and thus on the energy deposition, is by far the most important. There is however an increasing spread of the bolometric corrections towards 500 days which could be related to the local trapping of the positrons in these models. The energy deposition depends on the optical depth to the γ-rays as $L \propto e^{-\tau}$, which in turn depends on the ejecta mass as $\tau \propto M^2/E$. As the optical depth to the gamma rays decreases from ~1 on the early tail to $\ll$1 on the late tail the dependence on the intial mass is much stronger on the late tail. This behaviour is well followed by the models, which have similar luminosities on the early tail but differs with a factor of ~2 on the late tail. The choice of the initial mass is mainly motivated by the agreement with nebular spectra discussed in J14 but the lightcurve provides an additional constraint that further motivates this choice. There is a degeneracy however, between the initial mass and the mixing of the Fe/Co/He material which, as discussed below, have a similar effect on the tail luminosity. Therefore the constraint on the intial mass from the tail luminosity may in fact be weak. This degeneracy may, in turn, be broken by taking into account the diffusion phase lightcurve, for which the diffusion time depends on the mass as $t_d \propto (M^3/E)^{1/4}$, but in the end our restricted set of models prevents us to make any definite conclusions. The issue of degeneracy is better investigated by a quantative method like the one described in Sect. 4.6.

4.1.2. Marcoscopic mixing

The degree of macroscopic mixing may affect both the energy deposition (bolometric lightcurve) and the way this energy is processed (bolometric correction). Comparing models 13A and

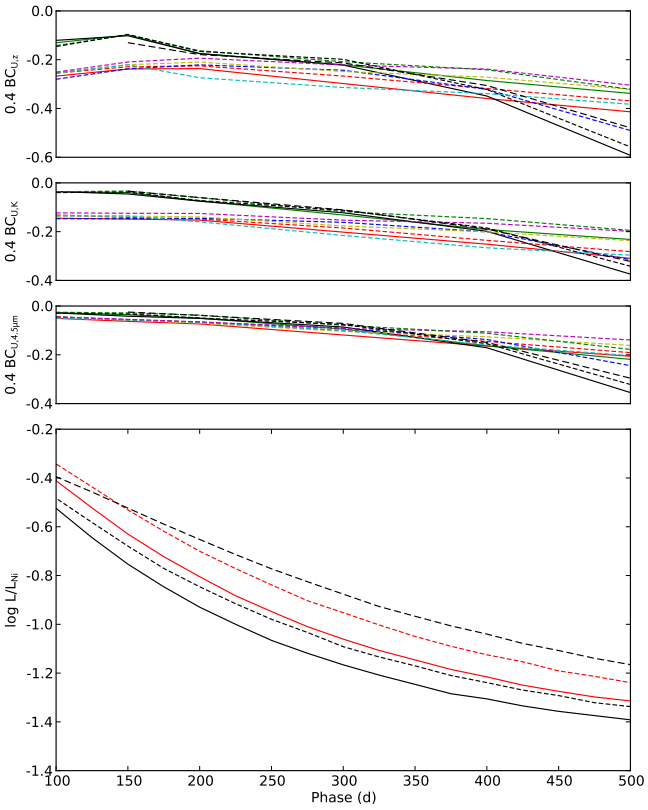

Fig. 21. Lower panel: 100-500 days bolometric lightcurves for the J14 models calculated with HYDE. The bolometric lightcurves have been normalized to the radioactive decay chain luminosity of 0.075 $M_\odot$ of ^{56}Ni and the models are displayed as follows; 12A (red solid line), 12B/C (black solid line), 13A/B (red short-dashed line), 13C/D/E/F/G (black short-dashed line), 17A (black long-dashed line). Upper panels: U to 4.5 μm, U to K and U to z bolometric corrections for the J14 models. The bolometric corrections have been multiplied with 0.4 to be on the same scale as the bolometric lightcurves and the models are displayed as follows; 12A (red solid line), 12B (green solid line), 12C (black solid line), 13A (red short-dashed line), 13B (blue short-dashed line), 13C (yellow short-dashed line), 13D (cyan short-dashed line), 13E (magenta short-dashed line), 13F (green short-dashed line), 13G (black short-dashed line), 17A (black long-dashed line).

13C that differs only in the degree of macroscopic mixing and the oxygen filling factor we find that the effect on the bolometric lightcurve, and thus on the energy deposition, is by far the most important. In general the mixing of the Fe/Co/He zone, containing the ^{56}Ni and its decay products, determines the overall deposition of the radioactive decay energy whereas the mixing of the other zones determines the distribution of this energy in each of these zones. We have used two configurations, one where all core zones (Fe/Co/He to O/C) are randomly mixed within 3500 km s^{-1} (medium), and one that differs only in that 50 percent of Fe/Co/He material have been mixed out in the helium zone within 3500-6000 km s^{-1} (strong). The mixing of the Fe/Co/He material affects the tail luminosity in a way similar to the initial mass, as the average optical depth to the γ-rays decreases if the Fe/Co/He material is distributed further out in the ejecta. Comparing the optimal model (12C) and model 12A, the optimal model with strong mixing is ∼10 percent fainter on the early tail increasing to ∼30 percent on the late tail. The mixing has an even more pronounced effect on the rise to peak luminosity, as the diffusion time for energy deposited further out in the ejecta is shorter. Comparing again the optimal model (12C) and model 12A, the optimal model with strong mixing show a much faster rise to peak luminosity and is in much better in agreement with observations. In Sect. 4.5 we show that the optimal hydrodynamical model also has strong mixing of the ^{56}Ni, which seems to be required to fit the rise to peak luminosity. The choice of the mixing is mainly motivated by the lightcurve and in particular by the rise to peak luminosity. Naively this choice is in contradiction with the small size of the Fe/Co/He zone (1600-2100 km s^{-1}) determined in Sect. 3.3.8. However, the amount of material distributed far out in the ejecta does not necessarily need to be high to reproduce the rise to peak luminosity. Further modelling with different distributions of the Fe/Co/He material is required to resolve this issue. Clearly there is a large number of possible configurations that have not been investigated, e.g. a configuration with partial mixing of the core zones, as we found evidence for in Sect. 3.3.

4.1.3. Filling factors

The filling factors may affect both the energy deposition (bolometric lightcurve) and the way this energy is processed (bolometric correction). However, in the optically thin limit, the energy deposition does not depend on the filling factors, as the total cross section of each zone remains the same. The differences in the bolometric lightcurves for models only differing in the filling factors (not shown) are negligible. However, as the fraction of the deposited energy going into heating, ionization and excitation is not particularly sensitive to the density (Kozma & Fransson 1992), there is reasons to suspect that the differences in the bolometric corrections are small as well. We have used a number of configurations, where the filling factor of the oxygen zones ranges from small (0.043) to large (0.19), and adjusted the filling factors of the other zones accordingly. Comparing the pseudo-bolometric lightcurves of models 13C and 13E, which differ only in the oxygen zone filling factor, these are indeed very similar, but show a small difference increasing to ∼10 percent towards 500 days. The choice of a small oxygen zone filling factor is motivated by the agreement with nebular spectra discussed in J14 and is also consistent with the constraint derived in J14 from the small scale fluctuations in the [O I] 6300 and Mg I] 4571 Å lines discussed in Sect. 3.3.10. Again there is a large number of possible configurations that have not been investigated.

4.1.4. Positron trapping

The positron trapping may affect both the energy deposition (bolometric lightcurve) and the way this energy is processed (bolometric correction). However, in our models the energy deposition does not depend on the positron trapping as the optical depths to free-streaming positrons are allways $\gg$1. Positron trapping only affects the bolometric corrections when the fraction of radioactive decay energy deposited by the positrons becomes significant, and before this models with locally trapped or free-streaming positrons are indistinguishable. Comparing the optimal model (12C) and model 12B, which differs only in the positron trapping, the bolometric corrections for the optimal model gets increasingly larger after ∼300 days, when the contribution from positrons to the energy deposition starts to become significant. The reason for this is that in the optimal model all positrons are trapped in the Fe/Co/He zone, and do not contribute to the heating of other zones, resulting in a lower lumi-

nosity in lines arising from these zones, in particular the strong [O I] 6300,6364 Å and Mg I] 4571 Å lines. The Fe/Co/He zone also has a lower temperature than other zones because of efficient cooling from the large number of iron lines, and the emission arising from this zone is redder. Not surprisingly, the effect on the U to z bolometric correction is strongest and begins earliest. The choice of local positron trapping for the optimal model (12C) is mainly motivated by the better fit to the pseudo-bolometric lightcurves after 300 days. As discussed in J14, the constraints derived from nebular spectra are not conclusive. However, further evidence is gained from the 678 day spectrum of SN 2011dh presented by Shivvers et al. (2013), which shows a dramatic change as compared to our last spectrum. Many strong lines arising from other core zones than the Fe/Co/He zone, as the [O I] 6300,6364 Å and [Ca II] 7291,7323 Å lines, have disappeared or diminished dramatically, which is consistent with a scenario where all the positrons are being trapped locally in the Fe/Co/He zone. !Move to J14?!

4.2. Dust absorption and emission

As discussed in Sect. 3.2 and seen in Fig. 7, there is a strong increase in the fractional MIR luminosity between ~100 and ~200 days. As also discussed in Sect. 3.2 and seen in Fig. 5, there is a significant increase in the decline rates of the U to K pseudo-bolometric lightcurve between ~100 and ~200 days, even more pronounced in the U to z pseudo-bolometric lightcurve (Fig. **??**), but less so in the U to 4.5 μm pseudo-bolometric lightcurve (Fig. **??**). This suggests that some process is re-distributing flux from the optical and NIR to the MIR during this period. One example of such a process is formation of dust in the ejecta, which would absorb the still quite hot radiation from the SN and re-emit it at a much lower temperature. However, a change of the lines dominating the cooling of the ejecta in some zone could cause a similar effect. As discussed in Sect. 3.2, an increasing excess in the MIR during this period is also seen in SN 1993J, but the corresponding increase in the decline rates of the U to K pseudo-bolometric lightcurve is not seen, which makes the interpretation less clear. However, circum stellar medium (CSM) interaction that would affect the lightcurve in the opposite way, could be important for SN 1993J already at this early phase.

Dust is included in the modelling in a simplified way, and is represented as a gray absorptive opacity in the core (Fe/Co/He to O/C) zones. The absorbed luminosity is re-emitted as blackbody emission from a homologously expanding surface, representing a number of optically thick dust clouds. The fractional area of this surface x_{dust}, as compared to the area of the core, is a free parameter in the modelling, and determines the temperature of the emitted blackbody radiation. Note that our treatment of dust absorption and emission is only consistent if the number of dust clouds is large and the filling factor of those is small. At the temperatures expected for dust emission ($\lesssim$2000 K), the luminosity will be increased in the MIR and partly in the NIR, and decreased by a factor roughly equal to the total optical depth of the dust in the optical.

Using our simplified dust model, we find a value of 0.25 for the optical depth of the dust to match the behaviour of the optical lightcurves (see above). The value of x_{dust} was derived by minimization of the sum of squares of the relative flux differences of model and observed K, 3.6 and 4.5 μm photometry at 200, 300, 400 and 500 days (excluding K when the NIR coverage ends). This gives a value of x_{dust} of 0.01, which corresponds to temperatures of 2000, 1100, 666 and 416 K at 200, 300, 400 and 500 days respectively. However, assuming a large number of dust clouds and a small filling factor, it is possible to show from the assumptions made that $\tau = 3/4 x_{dust}$, so this value of x_{dust} is not consistent with our assumptions. Furthermore, as seen in Fig. 20, the evolution of the MIR bands is not well reproduced by the optimal model (12C), although the discrepancy is much worse for the same model without dust (12D). The discrepancy in the 4.5 μm band could possibly be explained by additional flux from the CO fundamental band, but the discrepancy in the 3.6 μm band will remain. Clearly the simplified dust model used is not good enough to well explain the MIR evolution, and further work is needed to better understand the evolution in these bands. On the other hand, as seen in Fig. **??**, the optimal model (12C) gives a good fit to the evolution in the optical, in particular to the increased decline rates between 100 and 200 days, and does improve the discrepancy in the MIR considerably as compared to the same model without dust (12D).

As a further complication there might also be a contribution from heated CSM dust to the MIR emission. Helou et al. (2013) show that such a model could explain the early MIR evolution, whereas they fail to reproduce the late evolution. We have not investigated such models, but it is possible that a combination of emission from ejecta dust, CSM dust and molecules could well explain the MIR evolution. However, as the observational constraints are limited, it is not clear how to disentangle the contributions from these different sources from each other.

!We probably need to add an discussion of the abscence of blue-shifted line peaks at late times here!

4.3. Molecule emission

As discussed in E14a, there is an excess in the 4.5 μm band developing during the first hundred days, as compared to blackbody fits to the optical and NIR photometry. As seen in Fig. 8, this excess continues to develop after 100 days, and at ~600 days the 4.5 μm band is ~100 times brighter as compared to such a blackbody fit. Although the interpretation of a blackbody fit to nebular photometry is far from clear, we find a similar factor if we compare to synthetic photometry for the J14 models without dust absorption/emission and molecule cooling (Fig. 20). Clearly molecule (CO and SiO), dust or some other source of emission is needed to explain this discrepancy. However, even if we exclude other explanations, it is not easy to distinguish between a molecule and dust origin.

As discussed in Sect. 3.3.9, we detect CO first overtone emission at ~100 and ~200 days. This implies at least some contribution from CO fundamental band emission to the 4.5 μm flux. Knowledge of the fundamental to overtone band flux ratio would make an estimate of the contribution from fundamental band emission to the 4.5 μm flux possible. For SN 1987A this ratio was ~1 at 100 days, a few at 200 days, but increased dramatically to ~100 towards 500 days (Bouchet & Danziger 1993). As discussed in Sect. 3.3.9, we can set upper limits on the fundamental to overtone band flux ratio of ~15 and ~20 at ~100 and ~200 days respectively, so assuming the same flux ratios as for SN 1987A would suggest a minor contribution to the 4.5 μm flux from fundamental band emission at these epochs. However, this assumption is a bit dubious as the mass, density and composition of the ejecta is quite different for a Type IIb SN as compared to SN 1987A.

Molecule cooling is included in the modelling in a simplified way, and is represented as the fraction of the deposited radioactive decay energy emitted as molecule (CO and SiO) emission in the O/C and O/Si/S zones. This energy is then emitted as

CO and SiO fundamental and first overtone band emission, represented as square line profiles with the typical widths of these emission bands. The CO first overtone band overlaps with the K band and the CO fundamental and SiO first overtone bands with the 4.5 μm band. The ratios of the fundamental and first overtone band emission are assumed to be the same as for SN 1987A (Bouchet & Danziger 1993). We have used two configurations, one where the fraction of deposited radioactive decay energy emitted as molecule emission has been set to one, and one where this fraction has been set to zero.

Molecule cooling is an important parameter in the modelling, not only because it affects the flux in the K band and 4.5 μm bands. It also determines the fraction of the deposited radioactive decay energy available for line emission and the temperature in the O/C and O/Si/S zones. The observed CO first overtone emission at ~100 and ~200 days, implies that there is some molecule cooling in the O/C zone. Synthetic photometry on the J14 spectra for models with complete molecule cooling overproduce the 4.5 μm magnitudes (Fig. 20), suggesting the amount of molecule cooling in the O/C zone to be modest. The strong similarity of the [O I] 6300 and Mg I] 4571 Å line profiles suggests the contribution from the O/C and O/Si/S zones to the [O I] 6300 Å emission to be modest, in turn suggesting the amount of molecule cooling in the O/C and O/Si/S zones to be significant. The redshift of the Ca II 8662 Å lines suggests a significant contribution from the [C I] 8727 Å line, found to arise mainly !is this correct! from the O/C zone in J14, in turn suggesting the amount of molecule cooling in the O/C zone to be modest. We have chosen no molecule cooling for our optimal model, but in the O/C zone an intermediate amount of cooling seems to be more likely.

4.4. Time dependent effects and 500-750 days bolometric lightcurve

Figure 22 shows the U to MIR and U to z pseudo-bolometric lightcurves compared to the bolometric lightcurve, deposited ^{56}Co decay gamma-ray and positron luminosity and deposited ^{57}Co decay luminosity for the optimal steady-state NLTE model (12C). The optimal hydrodynamical model produces very similar results. It is evident from the figure, that the deposited ^{56}Co decay luminosity is dominated by the positron contribution after ~450 day, and that the observed 500-750 days pseudo-bolometric lightcurves are unlikely to be powered by the gamma-rays emitted in this decay. Shivvers et al. (2013) suggested that the SN has entered a phase powered by the positrons emitted in the ^{56}Co decay after 300-350 days. Given our results, this suggestion seems to be roughly correct in the sense that the positron contribution dominates the deposited luminosity after ~450 days. However, as we will discuss below, it is not clear that the positron contribution dominates the emitted luminosity, because there is a number of processes that could provide additional energy sources.

There is observational evidence for additional energy sources from the observed pseudo-bolometric lightcurves. The decline rates of the pseudo-bolometric lightcurves between 500 and 750 days is 0.0065-0.0070 mag s^{-1}, significantly lower than the decay rate of ^{56}Co. As discussed in Sect. 4.1, our optimal model requires the positrons to be locally trapped to fit the 300-500 days U to z pseudo-bolometric lightcurve. This implies an increasing contribution from the low temperature Fe/Co/He zone (Sect. 4.1), in turn implying an increasing bolometric correction. However, the ratio of the observed U to z pseudo-bolometric luminosity and the bolometric luminosity of the optimal steady-state NLTE model, increases from ~0.3 to ~0.5 between 450 and 750 days, in contradiction with this expectation.

If the recombination time scales become longer than the time scale of the ^{56}Co decay, the steady-state assumption required for the NLTE modelling is no longer valid. Some fraction of the deposited radioactive decay energy will then build up a reservoir of ionization energy, which through recombination emission could eventually dominate the emitted luminosity. This process is called freeze-out and, as discussed in J14, approximate calculations suggest that in the hydrogen-rich envelope freeze-out occurs already at 100-200 days and in the helium envelope at ~500 days !is this correct!. The contribution from the hydrogen envelope, which absorbs a negligible fraction of the radioactive decay energy, is likely to be small whereas the contribution from the helium envelope could very well be substantial. We use a time-dependent NLTE code (Kozma & Fransson 1992, 1998a,b) to test the steady-state assumption for our optimal steady-state NLTE model. Figure 23 shows the synthetic B, V, r and I band photometry, with and without a steady-state assumption, as modelled with this code. It is clear from the figure, that time-dependent effects start to become important at ~600 days, and after ~700 days recombination emission from the helium envelope provides a dominant and increasing contribution to the flux in these bands. To determine if the additional energy source provided by freeze-out in the helium envelope can fully explain the late-time evolution of the pseudo-bolometric lightcurves is outside the scope of this paper, but it is clear that this contribution is likely to be substantial. The 678 day spectrum of SN 2011dh presented by Shivvers et al. (2013) !Is this date correct, there is 2 spectra!, shows features not present in our last optical spectra that could be identified as the He I 6678 Å and 7065 Å lines, whereas the strong feature identified as Na I 5890,5896 Å by the authors could have a significant contribution from, or be fed by, the He I 5876 Å line. This is consistent with a substantial contribution from helium envelope recombination emission at this epoch.

CSM interaction became the dominant energy source at ~300 days for SN 1993J !reference!, giving rise to broad box-like Hα and Na I 5890,5896 Å lines and a considerable flattening of the lightcurves. The 678 day spectrum of SN 2011dh presented by Shivvers et al. (2013) !Is this date correct, there is 2 spectra! shows a feature that is interpreted as broad box-like Hα emission by the authors, but no broad box-like Na I 5890,5896 Å emission is seen. The interpretation of the broad feature as Hα emission is far from clear, as a number of other lines may contribute in this wavelength range (including the He I 6678 Å line discussed above), and the feature is also much weaker than for SN 1993J at a similar epoch. It is hard to exclude a contribution from CSM interaction to the emitted luminosity, but as the flatting of the lightcurve is seen in all optical bands as well as the MIR bands, and is actually least pronounced in the r band, we do not find it likely to be dominant.

Additional energy sources could also be provided by the decay of radioactive isotopes other than ^{56}Co. In the optimal steady-state NLTE model, the fractional luminosity deposited by the ^{57}Co decay is ~10 percent at 700 days and increasing. A higher mass of ejected ^{57}Co than assumed in the optimal steady-state NLTE model, can not be excluded, and could help explain the observed evolution. The fractional luminosity deposited by the decay chain of ^{44}Ti in the optimal steady-state NLTE model is negligible, but contributions from other isotopes not included in the modelling can not be excluded.

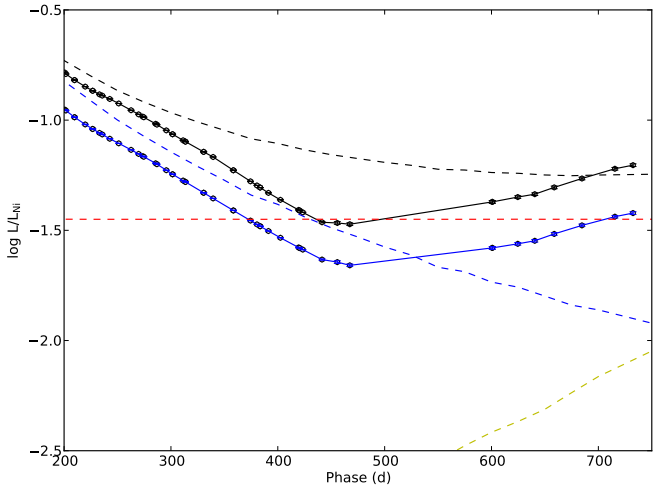

Fig. 22. U to MIR (black dots) and U to z (blue dots) pseudo-bolometric lightcurves compared to the bolometric lightcurve (black dashed line), deposited ^{56}Co decay gamma-ray (blue dashed line) and positron (red dashed line) luminosity and deposited ^{57}Co decay luminosity (yellow dashed line) for the optimal steady-state NLTE model (12C). The lightcurves have been normalized to the radioactive decay chain luminosity of 0.075 $M_\odot$ of ^{56}Ni.

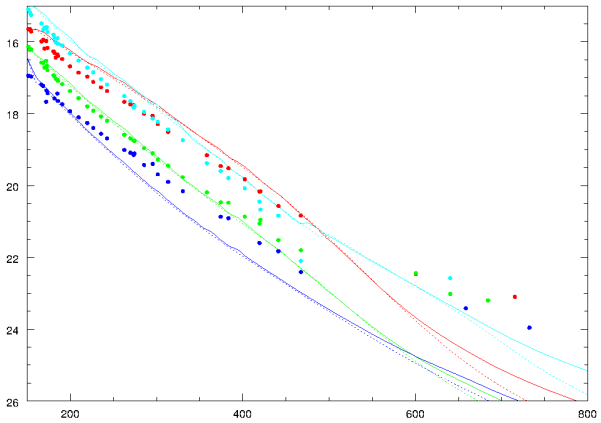

Fig. 23. Synthetic *B* (blue), *V* (yellow), *r* (red) and *I* (cyan) magnitudes for the optimal steady-state NLTE model (12C) as calculated with the time dependent NLTE code with (dashed lines) and without (solid lines) a steady-state assumption compared to the observed magnitudes (dots). !This figure has to be remade and does not show model 12C (but a similar model)!

4.5. Hydrodynamical modelling of the 0-100 days bolometric lightcurve

In this section we use the grid of SN models constructed with HYDE and MESA STAR presented in E14b and the procedure described therein to fit the 0-100 days bolometric lightcurves and photospheric velocities of SNe 2011dh, 1993J and 2008ax. The progenitor and SN parameters are the helium core mass (M_{He}), the explosion energy (E), the mass of ejected ^{56}Ni (M_{Ni}) and the distribution of it (Mix_{Ni}). The total parameter space spanned is M_{He}=2.5-7.0 $M_\odot$, E=0.4-2.2×10^{51} erg, M_{Ni}=0.05-0.250 $M_\odot$ and Mix_{Ni}=0.6-1.4 using a 15×10×9×9 grid. The stellar models consists of bare helium cores without a hydrogen envelope and as discussed in E14b this is sufficient to determine explosion energy, helium core mass and mass and distribution of the ejected ^{56}Ni. To estimate the radius modelling of the early cooling phase, which depends on the mass and radius of the hydrogen envelope, is necessary. The strenghth of our method as compared to previous hydrodynamical modelling is the ability to determine the errors in the derived quantities arising from errors in the observed quantities and constrain the degeneracy of the solutions found. As decribed in E14b equal weight is given to the diffusion phase lightcurve (5-40 days), the early tail lightcurve (40-100 days) and the early photospheric velocity evolution (5-40 days). The SNe modelled here constitutes the gold part of the Type IIb literature sample by virtue of the data quality and the hard constraints on their explosion epochs. In Ergon et al. (2014a) we model the silver part of this sample and the statistics for the complete sample is presented and discussed therein.

Figure 24 shows the model bolometric lightcurve and photospheric velocity evolution compared to the observed UV to MIR pseudo-bolometric lightcurve and velocity evolution for the absorption minimum of the Fe II 5169 Å line for the optimal models of SNe 2011dh, 2008ax and 1993J. The UV to MIR pseudo-bolometric lightcurves for SNe 2008ax and 1993J were constructed from the *U* to *K* pseudo-bolometric lightcurves assuming the same UV and MIR fractions as for SN 2011dh. Table 3 gives the helium core mass, explosion energy, mass of ejected ^{56}Ni and the distribution of it for the optimal models and the corresponding errors, calculated as described in E14b. The derived parameters for SN 2011dh are in good agreement with the results in B12. The helium core mass and explosion energy derived for SNe 1993J and 2008ax are similar to what is derived for SN 2011dh, whereas the mass of ejected ^{56}Ni differs significantly. The ^{56}Ni is distributed far out in the ejecta for all three SNe. The fraction of ^{56}Ni outside 3500 and 6000 km s^{-1} is 53 and 8 percent respectively for SN 2011dh. This is in rough agreement with the optimal NLTE model, altough in this model the ^{56}Ni is confined within 6000 km s^{-1}. We note that the velocity evolution of SN 2008ax is not well fitted, which could be explained by a worse correspondence between the absorption minimum of Fe II 5169 Å and the photosphere as compared to SNe 2011dh and 1993J. Figure 25 shows contour plots of the relative error in the fit as a function of helium core mass and energy. These contour plots show the degenaracy in the solutions found and, as discussed in E14b, there is as a strong degeneracy in helium core mass and explosion energy if the fitting is done using the bolometric lightcurve alone. The constraint from the photospheric velocity evolution decrease this degeneracy significantly and the fit becomes quite robust.

4.6. Hydrodynamical modelling of the 0-300 days bolometric lightcurve

In this section we extend the temporal coverage of the hydrodynamical model grid to 300 days (which is the period for which we have full *U* to 4.5 μm coverage), and make a fit of the observed *U* to 4.5 μm pseudo-bolometric lightcurve of SN 2011dh to this extended model grid. The method used is to calculate the bolometric lightcurve after 100 days using the HYDE code, assuming homologous expansion and instant emission of the energy deposited by the radioactive decay chains. However, to compare with the pseudo-bolometric lightcurve after 100 days, we also include a correction for the flux within the *U* to 4.5 μm wavelength range, determined with the steady-state NLTE code. The fitting is done by minimization of the square of the relative residuals, giving equal weight to the diffusion phase lightcurve (5-40 days), the early tail lightcurve (40-100 days), the late tail

Table 3. Helium core mass, explosion energy, mass of the ejected ^{56}Ni and the distribution of it for the optimal models of SNe 2011dh, 1993J and 2008ax.

SN	E (10^{51} erg)	M_{He} ($M_\odot$)	M_{Ni} ($M_\odot$)	Mix_{Ni}
2011dh	0.55 (+0.40,-0.15)	3.44 (+0.70,-0.26)	0.075 (+0.028,-0.020)	1.10 (+0.06,-0.00)
2008ax	0.70 (+0.50,-0.30)	3.19 (+0.56,-0.39)	0.175 (+0.087,-0.099)	0.93 (+0.04,-0.00)
1993J	0.60 (+0.45,-0.20)	3.31 (+0.60,-0.25)	0.106 (+0.034,-0.028)	0.90 (+0.24,-0.08)

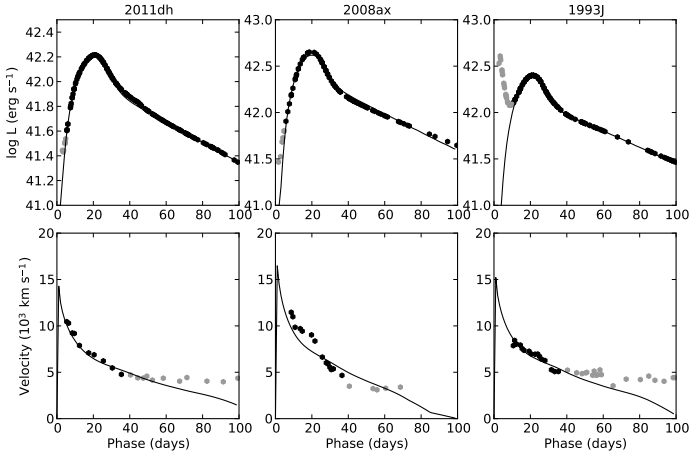

Fig. 24. Bolometric lightcurve (upper panels) and photospheric velocity evolution (lower panels) for the optimal models as compared to the observed UV to MIR pseudo-bolometric lightcurve and velocity evolution for the absorption minimum of the Fe II 5169 Å line for SNe 2011dh (left panels), 2008ax (middle panels) and 1993J (right panels).

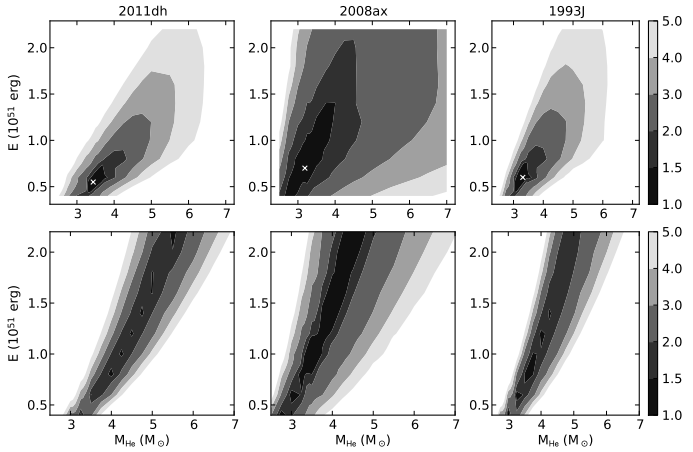

Fig. 25. Contour plots showing the standard deviation in the fits normalized to that of the optimal model projected onto the E-M_{He} plane for the case where the photospheric velocities were used (upper panels) and not used (lower panels) for SNe 2011dh (left panels), 2008ax (middle panels) and 1993J (right panels).

lightcurve (100-300 days) and the early photospheric velocity evolution (5-40 days). This weighting scheme give less weight to the photospheric velocities, but this is also motivated as we have additional information about the lightcurve.

The correction for the flux within the U to 4.5 μm wavelength range was determined by evolving a strongly restricted set of the ejecta models with the steady-state NLTE modelling. In most of the parameter space spanned this correction did not vary much, and the number of ejecta models were chosen as small as possible to get a reasonable precision (∼10 percent) using linear interpolations. To further restrict the number of ejecta models, we excluded those for which the average bolometric luminosity was more than 25 percent below the average observed U to 4.5 μm luminosity, using the lower error bars for the distance and extinction, as we know these would never make a good fit.

The method has its limitations and all the free parameters of the steady-state NLTE modelling which are not possible to map from the hydrodynamical modelling, as the degree of macroscopic mixing, the fraction of the energy going into molecule cooling in the O/C and O/Si zones and the amount of dust, have to be assigned some values. Here we have chosen to give these parameters the same values as for our optimal steady-state NLTE model (Sect. 4.1). On the other hand, the fractional flux within U to 4.5 μm does not vary much between the J14 ejecta models during the first 300 days, and as the optical depth to the γ-rays (and thus the deposited energy) depends on the ejecta mass as M^2/E, we do not expect the derived helium core mass to be very sensitive to changes in this fraction.

Figure 26 shows the model bolometric lightcurve and photospheric velocity evolution compared to the observed UV to MIR pseudo-bolometric lightcurve and velocity evolution for the absorption minimum of the Fe II 5169 Å line for the optimal model. The parameters of the optimal model are E=$0.55^{+0.40}_{-0.15}\times10^{51}$ erg, M_{He}=$3.38^{+0.58}_{-0.27}$ $M_\odot$, M_{Ni}=$0.075^{+0.028}_{-0.017}$ $M_\odot$ and Mix_{Ni}=$1.00^{+0.00}_{-0.00}$, in close agreement with the results from the 0-100 days bolometric lightcurve. Figure 26 also shows contour plots of the relative error in the fit as a function of helium core mass and energy. These are quite similar to those for the 0-100 days period shown in Fig. 25 so the additional information provided by the 100-300 days bolometric lightcurve is not sufficient to give a robust fit without the use of the photospheric velocity evolution.

!Work in progress. The variation of the bolometric correction in parameter space is not yet included and we always use the bolometric correction from the optimal NLTE model!

5. Discussion

5.1. The nature of the progenitor star

In M11, B12, E14a, J14 and this paper we investigate the nature of the progenitor star using a number of different and, at least partially, independent methods. In M11 we analyse direct observations of the star by comparison of the observed magnitudes to predictions from stellar atmosphere and evolutionary models.

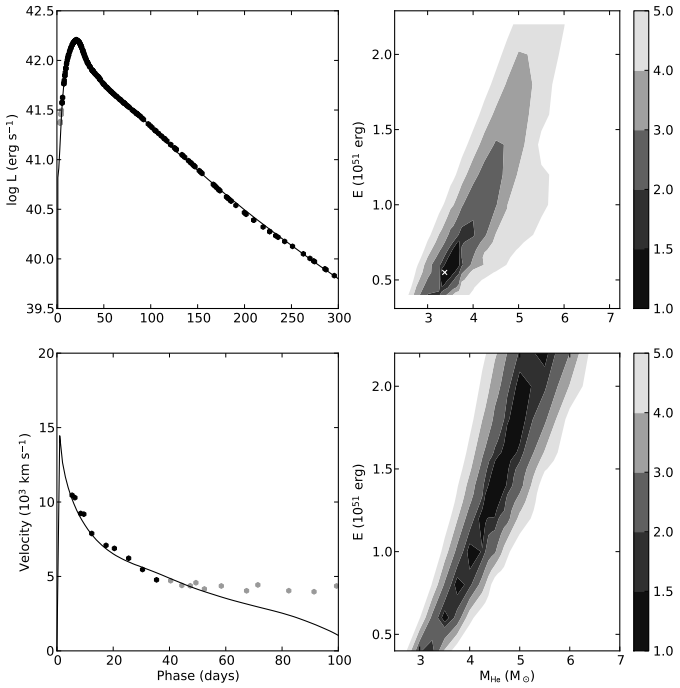

Fig. 26. Bolometric lightcurve (upper right panel) and photospheric velocity evolution (lower right panel) for the optimal model as compared to the observed UV to MIR pseudo-bolometric lightcurve and velocity evolution for the absorption minimum of the Fe II 5169 Å line. Observations not used in the fit are dispplayed in gre Contour plots showing the standard deviation in the fit normalized to that of the optimal model projected onto the E-M_{He} plane for the case where the photospheric velocities were used (upper left panel) and not used (lower left panel) are also shown.

The best match is found to be a yellow supergiant with an initial mass of 13±3 $M_\odot$ and a radius of ∼270 $R_\odot$. In E14a we present observations of the disappearance of this star, thus confirming that it was the progenitor of SN 2011dh.

In B12 and this paper we present hydrodynamical modelling, which shows that a star with a helium core of $3.3^{+0.6}_{-0.2}$ $M_\odot$ and a low-mass (∼0.1 $M_\odot$) and extended (200-300 $R_\odot$) hydrogen-rich envelope, exploding with an energy of $0.50^{+0.42}_{-0.10}\times10^{51}$ erg and ejecting $0.075^{+0.028}_{-0.013}$ $M_\odot$ of ^{56}Ni, mixed out to high velocities, well reproduces the observed bolometric lightcurve for the first 100 days.

In J14 and this paper we present steady-state NLTE modelling, which shows that a star with an initial mass of 12 $M_\odot$ well reproduces the observed 100-500 days spectral evolution and bolometric and photometric lightcurves. The evolution in the MIR however, which is complex and depends on both dust and molecule (CO and SiO) emission, is only partly reproduced. Particular attention is paid to the [O I] 6300,6364 Å line, which is very sensitive to the initial mass of the star. After ∼500 days we cannot reproduce the observed evolution of the pseudo-bolometric lightcurves, but it is clear from modelling using a time-dependent NLTE code (Kozma & Fransson 1992, 1998a,b), that in this phase freeze-out in the helium envelope is important and the assumption of steady-state is no longer valid.

In E14a we estimate a hydrogen mass of 0.01-0.04 $M_\odot$ using a Monte-Carlo atmosphere code, in agreement with the 0.024 $M_\odot$ estimated by Arcavi et al. (2011), using a similar but more advanced code, that included a NLTE treatment of hydrogen and helium. This hydrogen mass is consistent with the B12 ejecta model, and we also find the interface between the helium core and the hydrogen rich envelope to be located at a velocity consistent with this model.

As proposed in E14a and shown in E14b, the sensitivity of the mass and explosion energy derived from the hydrodynamical modelling to the errors in distance and extinction is weak, and merely effects the derived mass of ejected ^{56}Ni. Although we have not scanned the parameter space with the steady-state NLTE code, as this would be too computationally intensive, a similar conclusion is likely to hold for the initial mass as estimated from nebular spectra with the steady-state NLTE code. The use the hydrodynamical grid and the fitting procedure presented in E14b allows us to quantify the sensitivity of the results to errors in the photospheric velocities and, including errors in all the observables, the upper bound on the initial mass is found to be ∼15 $M_\odot$.

Overall the results obtained with the different methods are consistent and, even given the caveats of each individual method, it is likely that the progenitor star is of moderate initial mass (12-15 $M_\odot$), and has a low-mass extended hydrogen rich envelope, most of which must have been lost either through stellar winds or interaction with a binary companion. The moderate mass suggests that interaction with a binary companion is needed, as stellar winds of stars in this mass range are not strong enough to expell the hydrogen envelope before core-collapse. As we show in J14 and in this paper, using steady-state NLTE modelling of nebular spectra and hydrodynamical modelling of the bolometric lightcurve, SNe 2008ax and 1993J are likely to be of similar initial mass and have similar explosion energy as SN 2011dh, although the mass of the ejected ^{56}Ni may differ significantly depending on the adopted distance and extinction. In particular, the upper bound on the initial mass for all three SNe is found to be ∼15 $M_\odot$. For the same reason as discussed above, this suggests that interaction with a binary companion have taken place. In the case of SN 1993J, this conclusion is supported by direct observations of the binary companion (Maund et al. 2004). Observations, that could detect or set useful constraints on the presence of a companion star for SN 2011dh, are scheduled for Cycle 21 at HST, whereas similar observations for SN 2008ax would not be feasible, because of the longer distance. Clearly there is growing evidence that the main production channel for Type IIb SNe are stars whose hydrogen envelope has been stripped by interaction with a binary companion. Modelling of the nebular spectra and hydrodynamical modelling of the bolometric lightcurves for a larger sample of Type IIb SNe, could provide further evidence for this hypothesis.

6. Conclusions

We present two years of optical and NIR photometric and spectroscopic observations for the Type IIb SN 2011dh. Together with SWIFT UV and Spitzer MIR data we build a UV to MIR pseudo-bolometric lightcurve covering ∼750 days, although the photometric coverage ends at ∼100 days in UV and at ∼350 days in NIR. The spectral coverage ends at ∼200 days in NIR and ∼450 days in the optical.

We present 100-500 days bolometric and photometric lightcurves for the J14 steady-state NLTE models and discuss the constraints on the model parameters derived from those. To extend the temporal coverage of these models we construct 0-100 day bolometric lightcurves using HYDE (E14b) in homologous mode. The optimal 12 $M_\odot$ model, presented in J14 and chosen to give the best agreement with both spectra and lightcurves, agrees well with observations although the MIR evolution is only

partly reproduced. Strong mixing of the Fe/Co/He zone material is required to fit the rise to peak luminosity. The evolution of the tail luminosity also suggests strong mixing as well as a low (12 $M_\odot$) initial mass, although there is a degeneracy between those parameters. Local trapping of the positrons emitted in the ^{56}Co decay is required to fit the 300-500 days U to z pseudo-bolometric lightcurve. A modest amount of dust formed in the ejecta and no cooling from molecules (CO and SiO) gives the best fit to the optical and MIR photometric evolution. Modelling with a time-dependent NLTE code (Kozma & Fransson 1992, 1998a,b) shows that after ~600 days the steady-state assumption is no longer valid.

The suggestion by Shivvers et al. (2013), that the SN has entered a phase powered by the positrons emitted in the ^{56}Co decay after 300-350 days, is found to be roughly correct in the sense that the positron deposition dominates over the γ-ray deposition after ~450 days in our optimal steady-state NLTE model. However, there is both observational and theoretical evidence that the emitted flux is dominated by additional energy sources. The decline rates of the 500-750 days pseudo-bolometric lightcurves are significantly lower than the decay rate of ^{56}Co and the observed optical luminosity is ~50 percent of the bolometric luminosity in our optimal models, in contradiction with a scenario with locally trapped positrons. Modelling with the time-dependent NLTE code shows that after ~600 days freeze-out in the helium envelope becomes important, and recombination emission from the helium envelope is likely to contribute substantially to the observed luminosity. We find a substantial contribution from CSM interaction and other radioactive isotopes less likely.

We use the grid of hydrodynamical SN models presented in E14b and the procedure described therein to fit the 0-100 days bolometric lightcurves and photospheric velocities of SNe 2011dh, 1993J and 2008ax. This method allows us to determine the errors in the derived quantities arising from the uncertainties in distance, extinction and photospheric velocities. For SN 2011dh we find a helium core mass of $3.4^{+0.6}_{-0.3}$ $M_\odot$, an explosion energy of $0.55^{+0.40}_{-0.16}\times10^{51}$ erg and a mass of ejected ^{56}Ni of $0.075^{+0.028}_{-0.017}$ $M_\odot$, in agreement with our results from Bersten et al. (2012). For SNe 1993J and 2008ax we find values of the helium core mass and explosion energy similar to those of SN 2011dh, whereas the mass of ^{56}Ni depends sensitively on the adopted distance and extinction. Strong mixing of the ejected ^{56}Ni is required for all three SNe to fit the rise to peak luminosity. To extend the temporal coverage of the hydrodynamical grid to 300 days we apply a correction for the flux within the observed wavelength range (U to 4.5 μm) determined with the steady-stae NLTE modelling. This allows us to combine the power of our hydrodynamical model grid and the steady-state NLTE modelling. Applying this to the observed 3-300 days U to 4.5 μm pseudo-bolometric lightcurve of SN 2011dh, we find best fit values for the helium core mass, explosion energy, mass of ejected ^{56}Ni and the distribution of it in good agreement with those based on the 0-100 days bolometric lightcurve.

We find an excess in the MIR as compared to steady-state NLTE model photometry developing between 100 and 200 days, during which an increase in the optical tail decline rates is also observed. This behaviour could be reproduced by the steady-state NLTE modelling if a modest amount of dust (τ = 0.25) is being continuously formed in the ejecta during this period, although the photometric evolution in the MIR is only partly reproduced. As discussed in E14a an excess develops in the 4.5 μm band already during the first 100 days, which is unlikely to be caused by dust forming in the ejecta. CO fundamental band emission or emission from heated CSM dust, as proposed by Helou et al. (2013), are possible explanations. We detect CO first overtone band emission in NIR spectroscopy at 89 and 202 days implying a contribution to the 4.5 μm band flux from CO fundamental band emission at these epochs. The photometric evolution in the MIR is complex and might involve components from CO, SiO, ejecta and CSM dust emission for which, at the best, only a simple and approximate treatment is included in the steady-state NLTE modelling.

We estimate the sizes of the oxygen, magnesium, iron and [Ca II] 7291,7323 Å line emitting regions to 2900-3400, 2700-3600, 1600-2100 and 2100-2400 km s^{-1} respectively, in all compared cases smaller than those of SNe 1993J and 2008ax. Given the findings in J14, these regions would correspond to the oxygen, O/Ne/Mg, Fe/Co/He and Si/S nuclear burning zones and suggest partial mixing of the core material. The profiles of the [O I] 6300 Å and Mg I] 4571 Å lines show a remarkable similarity, suggesting that these lines arise from the same nuclear burning zone. Given the findings in J14, this would be the O/Ne/Mg zone and contributions from the O/Si/S and O/C zones to the [O I] 6300 Å flux would be modest. This suggests the amount of molecule (CO and SiO) cooling in these zones to be considerable. On the other hand, the overproduction of 4.5 μm flux in models with complete molecule cooling as well as the (possible) presence of the [C I] 8727 Å line, suggests this amount to be modest. Our optimal steady state NLTE model has no molecule cooling but an intermediate amount is probably more likely.

We use repetitions of small scale fluctuations in the [O I] 6300 Å and [O I] 6364 Å lines to find a line ratio close to 3, consistent with optically thin emission and in agreement with the results in J14, from 200 days and onwards. We also find the two strongest small scale features to repeat in the [O I] 5577 Å, O I 7774 Å and Na I 5890,5896 Å lines, suggesting these to be emitted, at least partly, by the same material. This is in agreement with the results in J14 where we find all these lines to have a significant contribution from the O/Ne/Mg zone.

We find a blue-shift of the center of flux of the [O I] 5577 Å, [O I] 6300 Å and Mg I] 4571 Å lines of ~1000 km s^{-1} or more decreasing towards zero at ~400 days. SNe 1993J and 2008ax show a similar blue-shift of these lines, but contrary to SN 2011dh it saturates at ~500 km s^{-1} from 200 days and onwards. For SNe 2011dh and 2008ax we find no significant blue-shift of the oxygen and magnesium lines in the NIR. In J14 we suggest the physical cause to the line-blocking in the core, based on results from the steady-state NLTE modelling, although this requires a different evolution of the core-opacity for SNe 1993J and 2008ax as compared to SN 2011dh.

This paper concludes our observational and modelling work on SN 2011dh presented in M11, B12, E14a and J14. We have applied stellar evolutionary progenitor analysis, hydrodynamical modelling, SN atmosphere modelling and steady-state NLTE modelling to our extensive set of observational data. Although a number of issues remains unsolved, as the photometric evolution in the MIR and the late time flattening of the lightcurve, the main characteristics of the SN and its progenitor star found by the different methods are consistent. The progenitor star appears to have been of moderate (12-15 $M_\odot$) initial mass, and the 3-4 $M_\odot$ helium core surrounded by a low-mass (~0.1 $M_\odot$) and extended (200-300 $R_\odot$) hydrogen-rich envelope. In particular we have found the initial masses of SNe 2011dh, 1993J and 2008ax to be $\lesssim$15 $M_\odot$, from both hydrodynamical modelling of the early bolometric evolution and steady-state NLTE modelling

of the late spectral evolution. This limit is also supported by stellar evolutionary progenitor analysis for SNe 2011dh and 1993J (Maund et al. 2004, 2011). Given that the mass-loss rates for stars in this mass range are probably not strong enough to expell the hydrogen envelope before core-collapse, a binary origin for these SNe is strongly suggested.

7. Acknowledgements

References

Arcavi, I., Gal-Yam, A., Yaron, O., et al. 2011, ApJ, 742, L18
Benvenuto, O. G., Bersten, M. C., & Nomoto, K. 2013, ApJ, 762, 74
Bersten, M. C., Benvenuto, O. G., Nomoto, K., et al. 2012, ApJ, 757, 31
Bouchet, P. & Danziger, I. J. 1993, A&A, 273, 451
Chugai, N. N. 1994, ApJ, 428, L17
Ergon, M., Jerkstrand, A., Bersten, M., Sollerman, J., & Fransson, C. 2014a, In preparation
Ergon, M., Sollerman, J., Fraser, M., et al. 2014b, A&A, 562, A17
Griga, T., Marulla, A., Grenier, A., et al. 2011, Central Bureau Electronic Telegrams, 2736, 1
Hammer, N. J., Janka, H.-T., & Müller, E. 2010, ApJ, 714, 1371
Helou, G., Kasliwal, M. M., Ofek, E. O., et al. 2013, ApJ, 778, L19
Jerkstrand, A., Ergon, M., Smartt, S., et al. 2014, In preparation
Jerkstrand, A., Fransson, C., & Kozma, C. 2011, A&A, 530, A45
Jerkstrand, A., Fransson, C., Maguire, K., et al. 2012, A&A, 546, A28
Kozma, C. & Fransson, C. 1992, ApJ, 390, 602
Kozma, C. & Fransson, C. 1998a, ApJ, 496, 946
Kozma, C. & Fransson, C. 1998b, ApJ, 497, 431
Matheson, T., Filippenko, A. V., Ho, L. C., Barth, A. J., & Leonard, D. C. 2000, AJ, 120, 1499
Maund, J. R., Fraser, M., Ergon, M., et al. 2011, ApJ, 739, L37
Maund, J. R., Smartt, S. J., Kudritzki, R. P., Podsiadlowski, P., & Gilmore, G. F. 2004, Nature, 427, 129
Maurer, I., Mazzali, P. A., Taubenberger, S., & Hachinger, S. 2010, MNRAS, 409, 1441
Milisavljevic, D., Fesen, R. A., Gerardy, C. L., Kirshner, R. P., & Challis, P. 2010, ApJ, 709, 1343
Podsiadlowski, P., Hsu, J. J. L., Joss, P. C., & Ross, R. R. 1993, Nature, 364, 509
Sahu, D. K., Anupama, G. C., & Chakradhari, N. K. 2013, MNRAS, 433, 2
Shivvers, I., Mazzali, P., Silverman, J. M., et al. 2013, ArXiv e-prints
Stancliffe, R. J. & Eldridge, J. J. 2009, MNRAS, 396, 1699
Stathakis, R. A., Dopita, M. A., Cannon, R. D., & Sadler, E. M. 1991, Supernovae, 649
Stritzinger, M., Hamuy, M., Suntzeff, N. B., et al. 2002, AJ, 124, 2100
Taubenberger, S., Navasardyan, H., Maurer, J. I., et al. 2011, MNRAS, 413, 2140
Taubenberger, S., Valenti, S., Benetti, S., et al. 2009, MNRAS, 397, 677
Tsvetkov, D. Y., Volkov, I. M., Baklanov, P., Blinnikov, S., & Tuchin, O. 2009, Peremennye Zvezdy, 29, 2
Tsvetkov, D. Y., Volkov, I. M., Sorokina, E., et al. 2012, Peremennye Zvezdy, 32, 6
Valenti, S., Fraser, M., Benetti, S., et al. 2011, MNRAS, 416, 3138
Van Dyk, S. D., Li, W., Cenko, S. B., et al. 2011, ApJ, 741, L28
Van Dyk, S. D., Zheng, W., Clubb, K. I., et al. 2013, ApJ, 772, L32
Woosley, S. E. & Heger, A. 2007, Phys. Rep., 442, 269
Yaron, O. & Gal-Yam, A. 2012, PASP, 124, 668

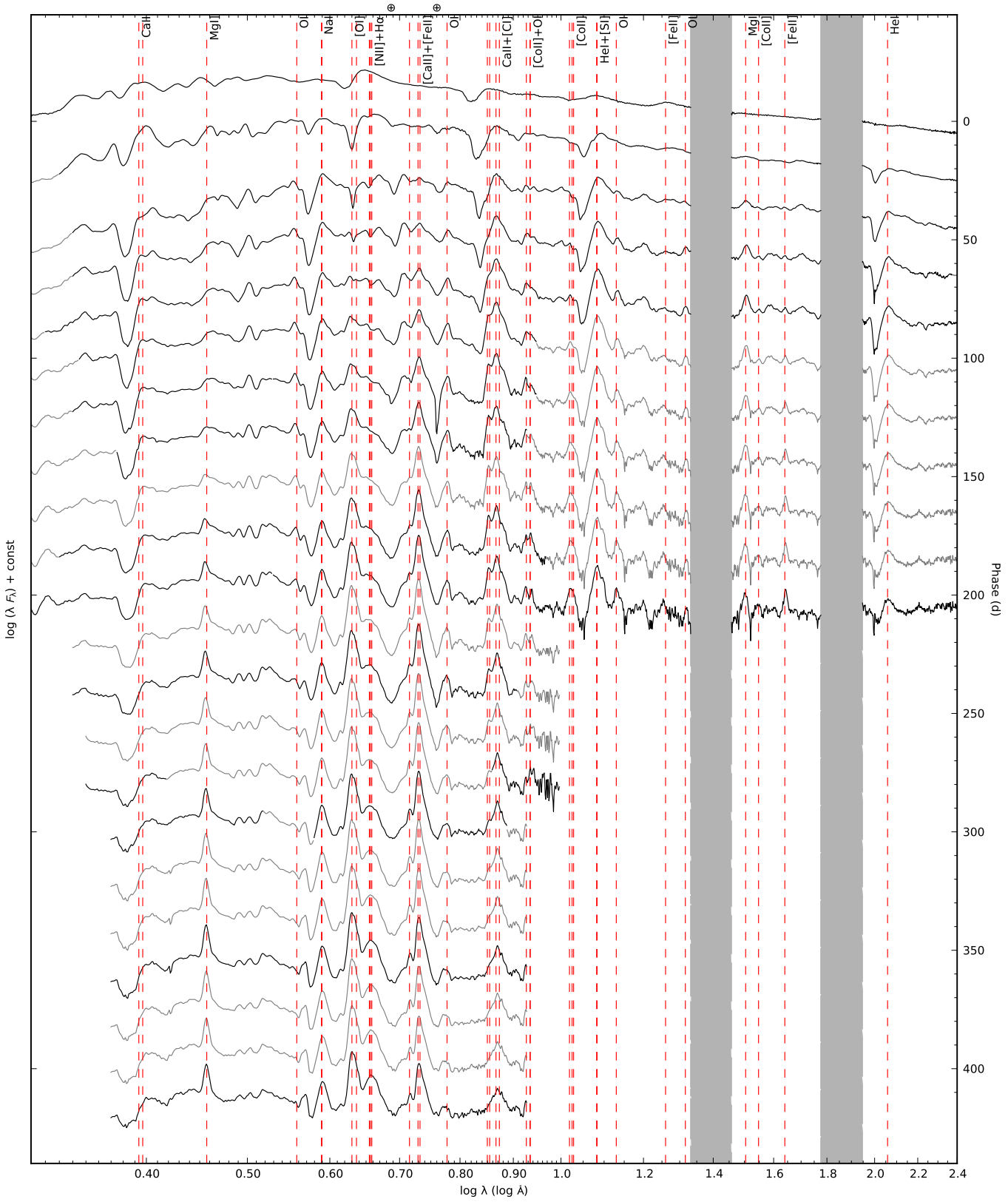

Fig. 2. Optical and NIR (interpolated) spectral evolution for SN 2011dh for days 5−425 with a 20-day sampling. Telluric absorption bands are marked with a ⊕ symbol in the optical and shown as grey regions in the NIR.

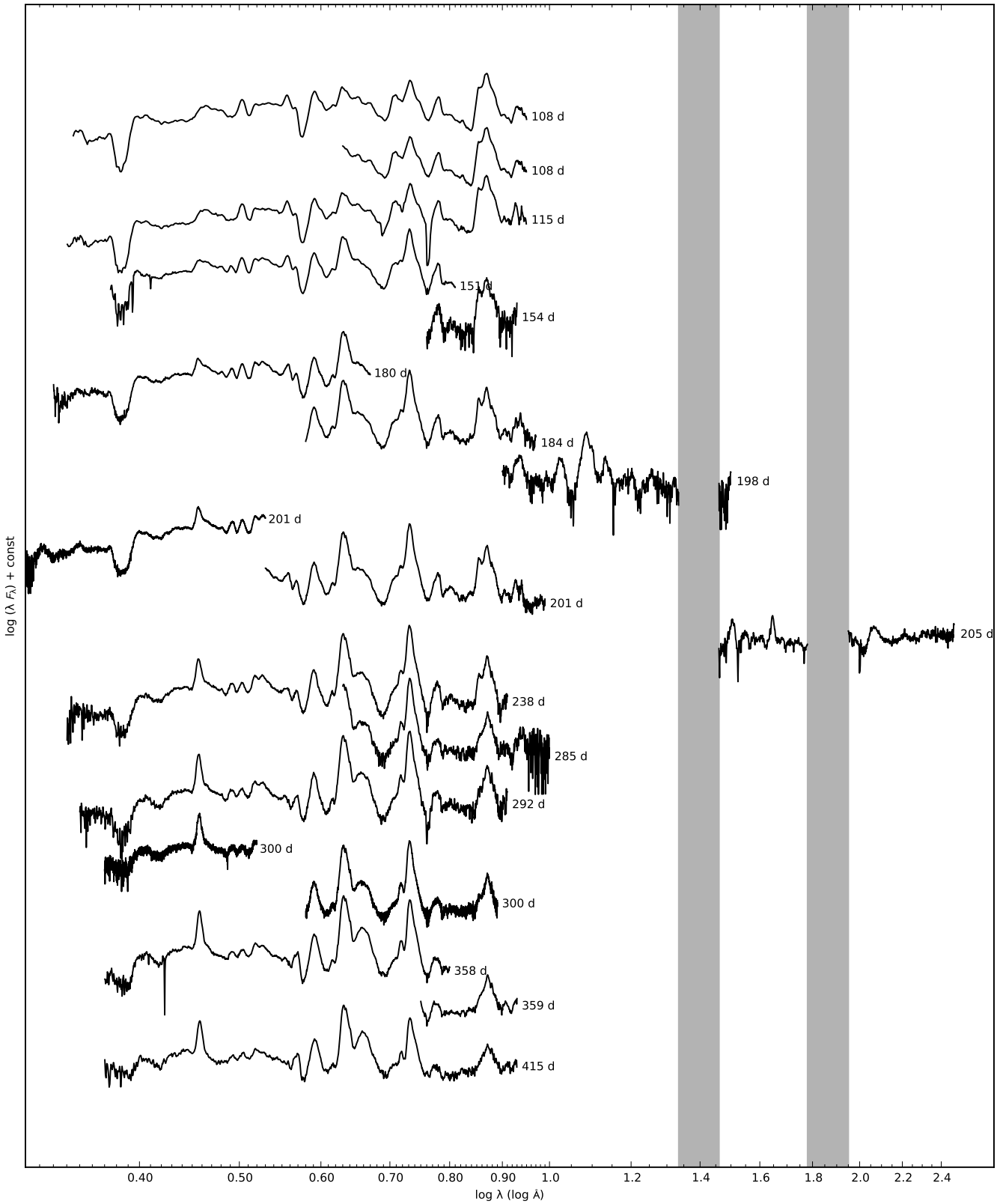

Fig. 3. Sequence of the observed late-time (100-415 days) spectra for SN 2011dh. Spectra obtained on the same night using the same telescope and instrument have been combined and each spectra have been labelled with the phase of the SN. Telluric absorption bands are marked with a ⊕ symbol in the optical and shown as grey regions in the NIR. !The AS-1.82/AFOSC spectra from 117 days is not yet included here.!

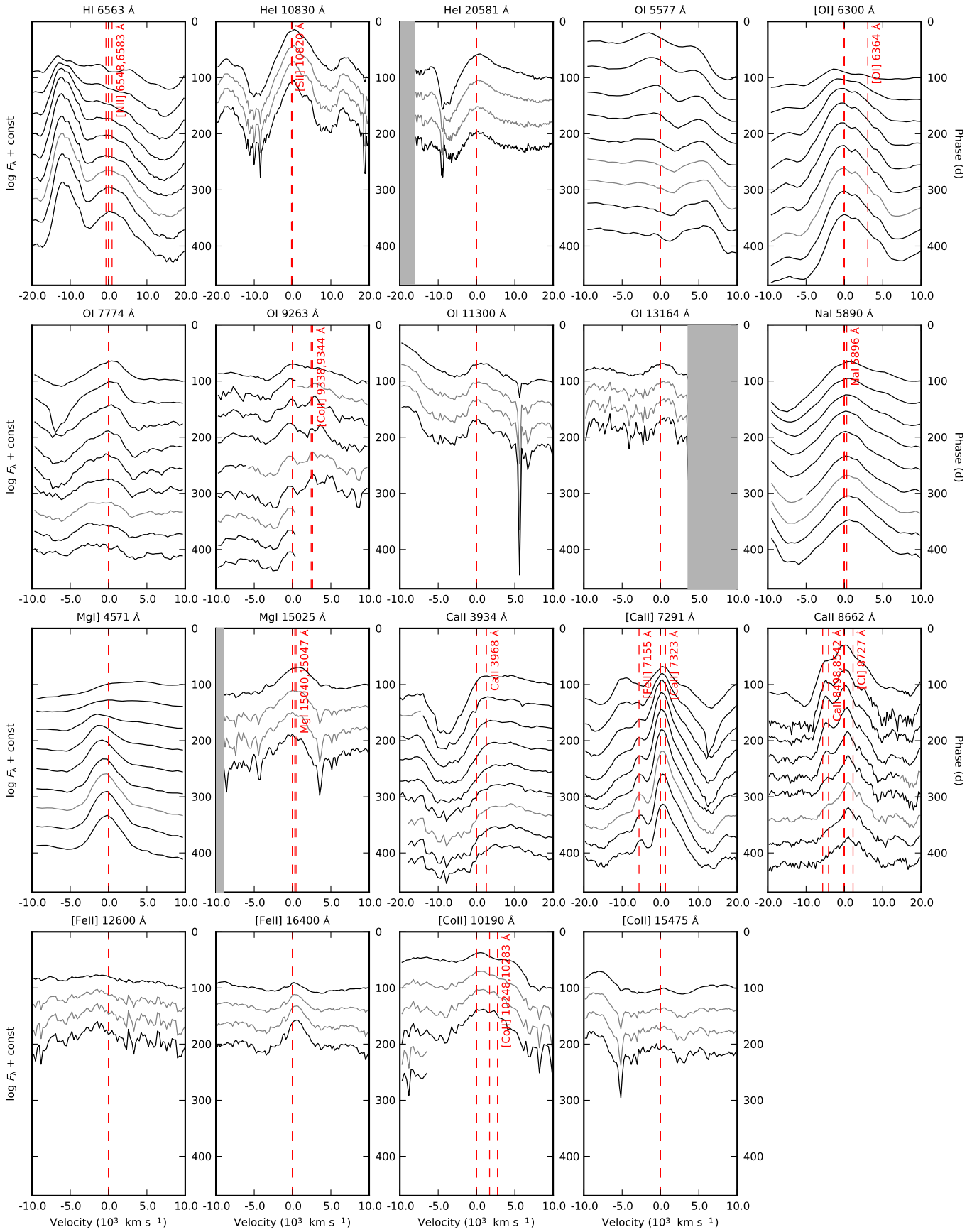

Fig. 9. Spectral evolution of all identified lines. Multiple or blended lines are marked with red dashed lines and telluric absorption bands in the NIR shown as grey regions.

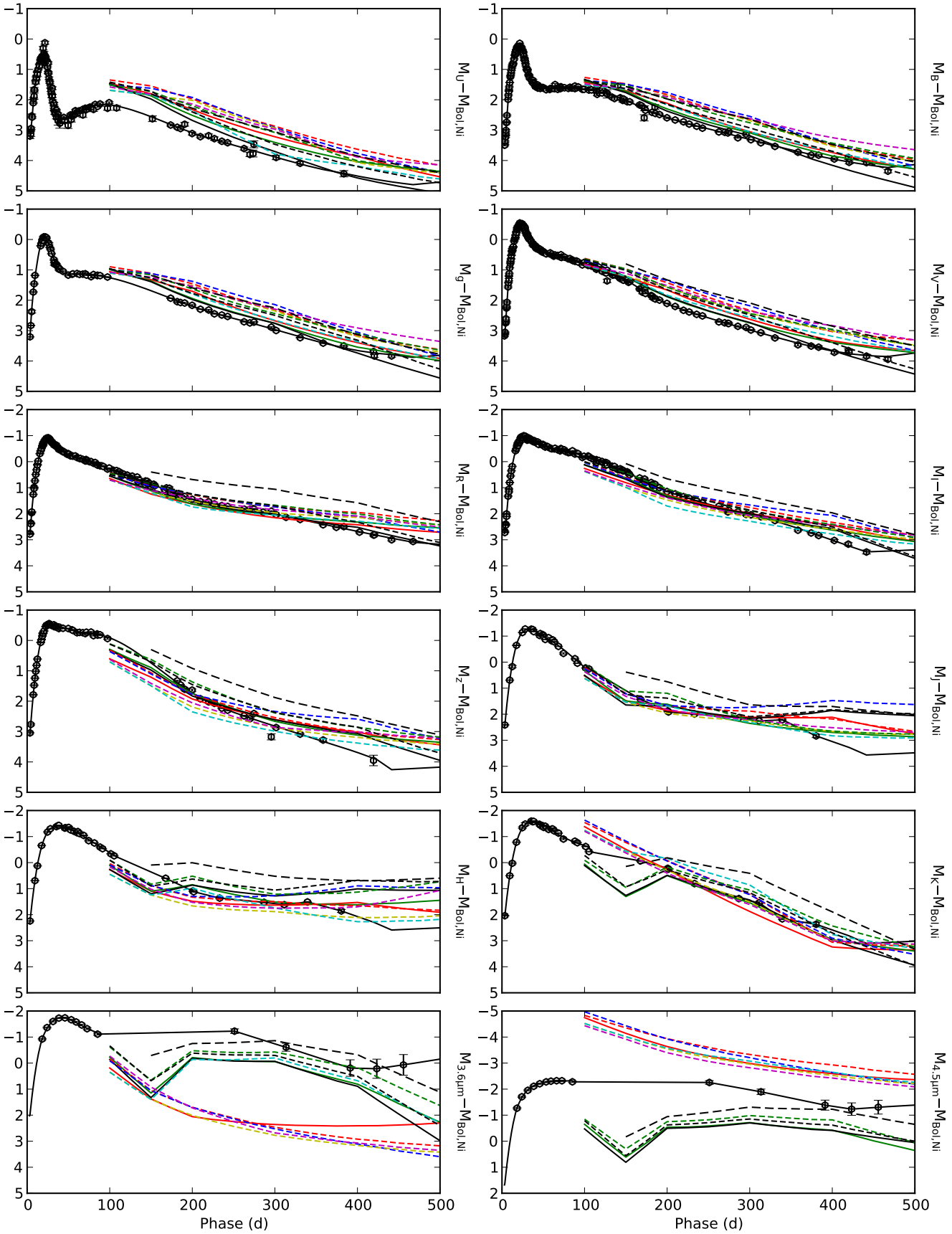

Fig. 20. Optical, NIR and MIR magnitudes for the J14 models as compared to the observed magnitudes. The lightcurves are displayed as in Fig. **??** and have been normalized to the radioactive decay chain luminosity of 0.075 $M_\odot$ of ^{56}Ni. The lightcurves shown in this figure and Fig. **??** and 20 have been normalized to the radioactive decay chain luminosity of 0.075 $M_\odot$ of ^{56}Ni.

Table 4. Optical colour-corrected JC *U* and S-corrected JC *BVRI* magnitudes for SN 2011dh. Errors are given in parentheses. For completeness data for the first 100 days already published in E14a are included. !One AFOSC observations from 2011-11-20 is not yet included in the table.!

JD (+2400000) (d)	Phase (d)	*U* (mag)	*B* (mag)	*V* (mag)	*R* (mag)	*I* (mag)	Telescope (Instrument)
55716.43	3.43	14.99 (0.03)	15.35 (0.02)	14.92 (0.02)	14.54 (0.01)	14.41 (0.02)	LT (RATCam)
55716.43	3.43	15.15 (0.08)	15.39 (0.02)	14.94 (0.02)	14.57 (0.01)	14.46 (0.01)	TNG (LRS)
55717.43	4.43	15.03 (0.03)	15.14 (0.02)	14.67 (0.03)	14.25 (0.01)	14.26 (0.03)	LT (RATCam)
55717.48	4.48	15.17 (0.09)	15.21 (0.03)	14.63 (0.03)	14.24 (0.01)	14.23 (0.02)	AS-1.82m (AFOSC)
55717.48	4.48	...	15.12 (0.03)	14.63 (0.02)	14.27 (0.01)	14.28 (0.02)	CANTAB (BIGST8)
55718.48	5.48	...	14.84 (0.01)	14.28 (0.02)	13.94 (0.01)	13.94 (0.01)	LT (RATCam)
55718.57	5.57	14.68 (0.06)	14.84 (0.02)	14.24 (0.02)	13.91 (0.01)	14.04 (0.01)	CA-2.2m (CAFOS)
55720.42	7.42	14.42 (0.02)	14.25 (0.01)	13.75 (0.03)	13.41 (0.01)	13.43 (0.02)	LT (RATCam)
55721.42	8.42	14.28 (0.10)	14.02 (0.01)	13.48 (0.01)	13.22 (0.01)	13.24 (0.02)	LT (RATCam)
55721.43	8.43	14.07 (0.07)	14.06 (0.01)	13.60 (0.04)	13.27 (0.02)	13.34 (0.02)	NOT (ALFOSC)
55722.42	9.42	...	13.86 (0.01)	13.29 (0.01)	13.05 (0.01)	13.07 (0.01)	LT (RATCam)
55723.41	10.41	13.98 (0.06)	13.71 (0.01)	13.16 (0.01)	12.89 (0.01)	12.90 (0.01)	LT (RATCam)
55724.41	11.41	13.91 (0.08)	13.62 (0.01)	13.03 (0.01)	12.79 (0.01)	12.77 (0.01)	LT (RATCam)
55725.39	12.39	...	...	12.94 (0.02)	12.66 (0.01)	...	MONTCAB (BIGST8)
55725.43	12.43	13.88 (0.07)	13.52 (0.02)	12.92 (0.04)	12.68 (0.01)	12.68 (0.01)	LT (RATCam)
55726.36	13.36	...	13.52 (0.01)	12.91 (0.02)	12.59 (0.01)	...	MONTCAB (BIGST8)
55728.40	15.40	...	13.39 (0.01)	12.77 (0.01)	12.44 (0.01)	...	MONTCAB (BIGST8)
55729.39	16.39	13.65 (0.01)	13.35 (0.01)	12.77 (0.06)	12.39 (0.01)	12.35 (0.02)	LT (RATCam)
55730.40	17.40	13.64 (0.03)	13.33 (0.01)	12.66 (0.01)	12.36 (0.01)	12.32 (0.01)	LT (RATCam)
55731.41	18.41	13.74 (0.09)	13.30 (0.01)	12.60 (0.02)	12.31 (0.01)	12.27 (0.01)	LT (RATCam)
55731.82	18.82	...	...	...	12.33 (0.02)	12.25 (0.01)	FTN (FS02)
55732.40	19.40	...	13.35 (0.03)	12.61 (0.01)	12.27 (0.01)	12.21 (0.01)	CANTAB (BIGST8)
55732.41	19.41	13.44 (0.06)	13.36 (0.02)	12.64 (0.02)	12.33 (0.02)	12.31 (0.02)	NOT (ALFOSC)
55732.46	19.46	13.71 (0.07)	13.32 (0.01)	12.58 (0.01)	12.28 (0.02)	12.22 (0.01)	LT (RATCam)
55733.45	20.45	13.67 (0.07)	...	...	12.26 (0.01)	12.20 (0.02)	LT (RATCam)
55734.52	21.52	13.37 (0.05)	13.33 (0.01)	12.58 (0.01)	12.25 (0.01)	12.29 (0.01)	CA-2.2m (CAFOS)
55735.44	22.44	13.91 (0.04)	...	...	12.26 (0.01)	12.16 (0.01)	LT (RATCam)
55736.44	23.44	14.13 (0.08)	...	...	12.26 (0.01)	12.16 (0.01)	LT (RATCam)
55737.39	24.39	...	13.65 (0.01)	12.72 (0.01)	...	...	LT (RATCam)
55738.42	25.42	14.50 (0.04)	13.79 (0.02)	12.81 (0.01)	12.32 (0.02)	12.22 (0.01)	LT (RATCam)
55738.51	25.51	14.20 (0.04)	13.77 (0.02)	12.82 (0.01)	12.38 (0.01)	12.26 (0.01)	NOT (ALFOSC)
55739.43	26.43	14.73 (0.04)	13.95 (0.02)	12.88 (0.01)	12.38 (0.01)	12.23 (0.01)	LT (RATCam)
55740.36	27.36	...	14.09 (0.04)	12.93 (0.01)	12.45 (0.01)	12.29 (0.01)	MONTCAB (BIGST8)
55740.43	27.43	14.91 (0.03)	14.12 (0.01)	12.97 (0.01)	12.48 (0.01)	12.30 (0.01)	LT (RATCam)
55740.44	27.44	...	...	12.97 (0.01)	12.47 (0.01)	...	TJO (MEIA)
55741.44	28.44	...	...	...	12.54 (0.01)	12.32 (0.01)	LT (RATCam)
55742.49	29.49	15.33 (0.01)	...	...	12.62 (0.01)	12.40 (0.01)	LT (RATCam)
55743.41	30.41	...	14.53 (0.01)	13.27 (0.02)	...	...	LT (RATCam)
55743.42	30.42	15.18 (0.05)	14.51 (0.02)	...	12.65 (0.01)	12.53 (0.01)	CA-2.2m (CAFOS)
55743.42	30.42	15.43 (0.05)	14.53 (0.01)	13.26 (0.03)	12.68 (0.01)	12.49 (0.01)	NOT (ALFOSC)
55745.39	32.39	15.74 (0.03)	14.74 (0.01)	13.44 (0.01)	12.77 (0.01)	12.56 (0.01)	NOT (ALFOSC)
55745.44	32.44	15.93 (0.04)	...	...	12.81 (0.01)	12.53 (0.01)	LT (RATCam)
55745.80	32.80	...	...	...	12.80 (0.01)	12.51 (0.01)	FTN (FS02)
55746.45	33.45	16.07 (0.04)	14.87 (0.03)	13.51 (0.01)	12.83 (0.01)	12.55 (0.02)	LT (RATCam)
55747.44	34.44	16.12 (0.04)	...	...	12.89 (0.01)	12.59 (0.01)	LT (RATCam)
55748.43	35.43	16.02 (0.02)	14.97 (0.01)	13.62 (0.01)	12.88 (0.01)	12.65 (0.01)	NOT (ALFOSC)
55748.44	35.44	16.27 (0.04)	...	...	12.94 (0.01)	12.62 (0.01)	LT (RATCam)
55750.40	37.40	16.20 (0.04)	15.10 (0.01)	13.73 (0.01)	13.03 (0.01)	12.73 (0.01)	NOT (ALFOSC)
55750.42	37.42	16.41 (0.14)	15.11 (0.02)	13.78 (0.03)	13.03 (0.01)	12.73 (0.02)	LT (RATCam)
55751.41	38.41	...	15.14 (0.01)	13.81 (0.01)	13.08 (0.01)	12.73 (0.01)	TJO (MEIA)
55751.43	38.43	...	...	...	13.11 (0.01)	12.77 (0.01)	LT (RATCam)
55752.45	39.45	16.54 (0.16)	...	...	13.13 (0.01)	12.75 (0.01)	LT (RATCam)

Table 3. Continued.

JD (+2400000) (d)	Phase (d)	U (mag)	B (mag)	V (mag)	R (mag)	I (mag)	Telescope (Instrument)
55753.42	40.42	...	15.29 (0.01)	13.90 (0.02)	...	...	LT (RATCam)
55753.46	40.46	16.45 (0.05)	15.24 (0.01)	13.86 (0.01)	13.15 (0.01)	12.81 (0.01)	NOT (ALFOSC)
55755.40	42.40	16.42 (0.04)	15.30 (0.01)	13.96 (0.01)	13.23 (0.01)	12.89 (0.01)	NOT (ALFOSC)
55756.44	43.44	...	15.28 (0.02)	13.98 (0.02)	13.28 (0.02)	12.86 (0.01)	AS-Schmidt (SBIG)
55756.45	43.45	...	15.38 (0.02)	13.98 (0.01)	13.27 (0.03)	12.92 (0.01)	LT (RATCam)
55757.43	44.43	16.42 (0.04)	15.38 (0.01)	14.05 (0.01)	13.29 (0.01)	12.97 (0.01)	NOT (ALFOSC)
55759.45	46.45	...	15.44 (0.01)	14.06 (0.02)	...	...	LT (RATCam)
55761.40	48.40	...	15.44 (0.01)	14.17 (0.01)	13.44 (0.01)	13.02 (0.01)	AS-Schmidt (SBIG)
55762.41	49.41	...	15.45 (0.01)	14.16 (0.01)	13.44 (0.01)	13.06 (0.01)	NOT (ALFOSC)
55762.78	49.78	...	...	...	13.44 (0.01)	13.03 (0.01)	FTN (FS02)
55763.44	50.44	...	15.47 (0.01)	14.22 (0.01)	13.47 (0.01)	13.09 (0.01)	AS-Schmidt (SBIG)
55765.43	52.43	16.44 (0.03)	15.52 (0.01)	14.26 (0.01)	13.55 (0.01)	13.17 (0.01)	NOT (ALFOSC)
55767.43	54.43	16.50 (0.05)	...	...	13.58 (0.01)	13.16 (0.02)	LT (RATCam)
55768.45	55.45	16.48 (0.04)	...	...	13.60 (0.02)	13.19 (0.02)	LT (RATCam)
55771.40	58.40	16.37 (0.03)	15.58 (0.01)	14.32 (0.01)	13.62 (0.01)	13.28 (0.01)	CA-2.2m (CAFOS)
55773.39	60.39	16.45 (0.04)	15.60 (0.01)	14.38 (0.01)	13.71 (0.01)	13.32 (0.01)	NOT (ALFOSC)
55776.38	63.38	16.47 (0.04)	15.64 (0.01)	14.46 (0.01)	13.77 (0.01)	13.36 (0.01)	NOT (ALFOSC)
55777.33	64.33	...	15.52 (0.03)	14.46 (0.02)	13.78 (0.02)	13.34 (0.02)	AS-Schmidt (SBIG)
55780.40	67.40	16.42 (0.03)	15.65 (0.01)	14.50 (0.01)	13.85 (0.01)	13.43 (0.01)	NOT (ALFOSC)
55783.43	70.43	16.41 (0.03)	15.71 (0.01)	14.58 (0.01)	13.94 (0.01)	13.51 (0.01)	NOT (ALFOSC)
55784.33	71.33	...	15.66 (0.02)	14.59 (0.01)	...	13.43 (0.02)	AS-Schmidt (SBIG)
55784.39	71.39	16.45 (0.04)	15.66 (0.01)	14.52 (0.02)	13.90 (0.01)	13.47 (0.02)	CA-2.2m (CAFOS)
55784.77	71.77	...	...	...	13.93 (0.02)	13.45 (0.01)	FTN (FS02)
55785.36	72.36	...	15.70 (0.02)	14.61 (0.01)	13.96 (0.01)	13.45 (0.01)	AS-Schmidt (SBIG)
55788.41	75.41	...	...	...	14.02 (0.02)	13.52 (0.01)	AS-Schmidt (SBIG)
55790.38	77.38	16.45 (0.09)	...	...	14.03 (0.01)	13.61 (0.01)	LT (RATCam)
55793.37	80.37	16.55 (0.07)	15.80 (0.01)	14.74 (0.01)	14.13 (0.01)	13.67 (0.01)	NOT (ALFOSC)
55795.35	82.35	16.40 (0.04)	15.78 (0.01)	14.76 (0.01)	14.12 (0.01)	13.68 (0.01)	CA-2.2m (CAFOS)
55797.37	84.37	...	15.83 (0.02)	14.82 (0.01)	...	...	AS-Schmidt (SBIG)
55797.76	84.76	...	...	...	14.22 (0.01)	13.68 (0.01)	FTN (FS02)
55798.36	85.36	16.50 (0.03)	15.84 (0.01)	14.84 (0.01)	14.25 (0.01)	13.65 (0.02)	NOT (ALFOSC)
55799.33	86.33	...	15.82 (0.01)	14.86 (0.01)	...	...	AS-Schmidt (SBIG)
55801.36	88.36	16.44 (0.04)	15.89 (0.01)	14.90 (0.01)	14.31 (0.01)	13.80 (0.01)	NOT (ALFOSC)
55801.40	88.40	...	15.80 (0.02)	14.90 (0.01)	...	...	AS-Schmidt (SBIG)
55803.35	90.35	...	15.88 (0.02)	14.91 (0.01)	14.32 (0.01)	13.79 (0.01)	AS-Schmidt (SBIG)
55805.33	92.33	...	15.87 (0.02)	14.97 (0.02)	14.37 (0.01)	13.83 (0.01)	AS-Schmidt (SBIG)
55810.34	97.34	16.68 (0.06)	16.00 (0.01)	15.11 (0.01)	14.52 (0.01)	14.02 (0.01)	NOT (ALFOSC)
55812.33	99.33	16.51 (0.03)	16.02 (0.01)	15.05 (0.01)	14.49 (0.01)	14.00 (0.01)	CA-2.2m (CAFOS)
55817.35	104.35	...	16.02 (0.03)	15.19 (0.02)	14.63 (0.02)	14.04 (0.02)	AS-Schmidt (SBIG)
55818.33	105.33	...	16.10 (0.02)	15.19 (0.02)	14.66 (0.01)	14.08 (0.01)	AS-Schmidt (SBIG)
55821.31	108.31	16.77 (0.08)	16.12 (0.02)	15.25 (0.01)	14.68 (0.01)	14.16 (0.01)	CA-2.2m (CAFOS)
55824.32	111.32	...	...	15.31 (0.02)	14.75 (0.03)	14.24 (0.03)	AS-Schmidt (SBIG)
55827.33	114.33	...	16.16 (0.03)	15.42 (0.01)	14.87 (0.02)	14.27 (0.01)	AS-Schmidt (SBIG)
55827.48	114.48	...	16.22 (0.07)	15.37 (0.03)	14.94 (0.05)	14.38 (0.05)	AT (ANDOR)
55828.27	115.27	...	16.34 (0.04)	15.39 (0.02)	14.86 (0.02)	14.31 (0.01)	AT (ANDOR)
55830.28	117.28	...	16.30 (0.02)	15.38 (0.01)	14.91 (0.01)	14.34 (0.01)	AS-1.82m (AFOSC)
55834.26	121.26	...	16.23 (0.03)	15.49 (0.02)	14.99 (0.02)	14.44 (0.02)	AT (ANDOR)
55834.31	121.31	...	16.35 (0.02)	15.55 (0.01)	14.99 (0.02)	14.41 (0.02)	AS-Schmidt (SBIG)
55838.34	125.34	...	...	15.64 (0.02)	15.11 (0.03)	14.49 (0.01)	AS-Schmidt (SBIG)
55839.28	126.28	...	16.39 (0.03)	15.65 (0.02)	15.12 (0.02)	14.52 (0.02)	AS-Schmidt (SBIG)
55840.26	127.26	...	16.44 (0.03)	15.57 (0.02)	15.15 (0.03)	14.53 (0.02)	AT (ANDOR)
55840.30	127.30	...	16.44 (0.14)	15.93 (0.06)	15.08 (0.04)	14.59 (0.04)	AS-Schmidt (SBIG)

Table 3. Continued.

JD (+2400000) (d)	Phase (d)	U (mag)	B (mag)	V (mag)	R (mag)	I (mag)	Telescope (Instrument)
55846.26	133.26	...	16.60 (0.03)	15.77 (0.02)	15.17 (0.02)	14.71 (0.02)	AT (ANDOR)
55847.30	134.30	...	...	15.81 (0.02)	15.35 (0.03)	14.77 (0.02)	AT (ANDOR)
55849.26	136.26	...	16.68 (0.05)	15.81 (0.02)	15.33 (0.03)	14.75 (0.02)	AT (ANDOR)
55853.27	140.27	...	16.32 (0.06)	15.90 (0.05)	15.44 (0.05)	14.91 (0.04)	AS-Schmidt (SBIG)
55855.38	142.38	...	...	15.96 (0.03)	15.44 (0.03)	14.93 (0.03)	AT (ANDOR)
55856.24	143.24	...	16.72 (0.06)	16.01 (0.03)	15.42 (0.02)	14.91 (0.02)	AT (ANDOR)
55858.29	145.29	...	...	16.02 (0.03)	15.45 (0.03)	14.96 (0.02)	AT (ANDOR)
55859.23	146.23	...	16.84 (0.05)	16.08 (0.02)	15.56 (0.03)	15.01 (0.02)	AT (ANDOR)
55860.22	147.22	...	16.80 (0.05)	16.10 (0.03)	15.53 (0.03)	15.02 (0.02)	AT (ANDOR)
55864.69	151.69	17.55 (0.09)	16.94 (0.02)	16.14 (0.01)	15.65 (0.01)	15.10 (0.01)	AS-1.82m (AFOSC)
55866.28	153.28	...	...	16.23 (0.02)	15.64 (0.03)	15.18 (0.02)	AT (ANDOR)
55867.70	154.70	...	16.97 (0.02)	16.21 (0.03)	15.71 (0.02)	15.25 (0.02)	CA-2.2m (CAFOS)
55879.66	166.66	...	17.19 (0.03)	16.58 (0.02)	15.99 (0.02)	15.49 (0.02)	AS-Schmidt (SBIG)
55881.74	168.74	...	17.23 (0.02)	16.59 (0.02)	15.94 (0.01)	15.66 (0.03)	CA-2.2m (CAFOS)
55883.24	170.24	...	...	16.72 (0.05)	16.19 (0.05)	15.61 (0.02)	AT (ANDOR)
55885.21	172.21	...	17.67 (0.10)	16.53 (0.03)	15.98 (0.05)	15.62 (0.03)	AT (ANDOR)
55885.73	172.73	...	17.36 (0.08)	16.67 (0.02)	...	15.59 (0.03)	AS-1.82m (AFOSC)
55886.75	173.75	17.97 (0.03)	17.43 (0.01)	16.79 (0.01)	16.17 (0.01)	15.73 (0.01)	NOT (ALFOSC)
55893.71	180.71	...	...	16.93 (0.02)	16.27 (0.01)	15.80 (0.02)	AS-Schmidt (SBIG)
55894.76	181.76	18.12 (0.03)	17.58 (0.01)	16.96 (0.01)	16.31 (0.01)	15.89 (0.01)	NOT (ALFOSC)
55896.20	183.20	...	...	17.03 (0.05)	16.44 (0.06)	16.01 (0.04)	AT (ANDOR)
55898.19	185.19	...	17.44 (0.08)	17.06 (0.04)	16.35 (0.04)	15.90 (0.03)	AT (ANDOR)
55898.73	185.73	18.20 (0.04)	17.65 (0.01)	17.09 (0.01)	16.39 (0.01)	16.05 (0.01)	NOT (ALFOSC)
55903.76	190.76	18.11 (0.06)	17.74 (0.02)	17.18 (0.02)	16.48 (0.01)	16.10 (0.02)	NOT (ALFOSC)
55912.79	199.79	18.51 (0.05)	17.93 (0.02)	17.37 (0.01)	16.68 (0.01)	16.33 (0.01)	NOT (ALFOSC)
55922.76	209.76	18.70 (0.03)	18.10 (0.01)	17.57 (0.01)	16.86 (0.01)	16.52 (0.01)	NOT (ALFOSC)
55932.79	219.79	18.77 (0.06)	18.26 (0.01)	17.80 (0.02)	16.97 (0.02)	16.72 (0.02)	NOT (ALFOSC)
55939.73	226.73	18.93 (0.05)	18.40 (0.02)	17.92 (0.02)	17.12 (0.01)	16.85 (0.01)	NOT (ALFOSC)
55948.73	235.73	19.11 (0.04)	18.56 (0.01)	18.08 (0.01)	17.27 (0.01)	17.04 (0.01)	NOT (ALFOSC)
55955.76	242.76	19.23 (0.04)	18.69 (0.01)	18.20 (0.01)	17.37 (0.01)	17.19 (0.01)	NOT (ALFOSC)
55975.69	262.69	19.61 (0.05)	19.01 (0.01)	18.59 (0.01)	17.67 (0.01)	17.51 (0.01)	NOT (ALFOSC)
55982.74	269.74	19.88 (0.07)	19.09 (0.02)	18.69 (0.02)	17.74 (0.01)	17.65 (0.01)	NOT (ALFOSC)
55986.62	273.62	19.88 (0.11)	19.15 (0.03)	18.75 (0.03)	17.76 (0.02)	17.83 (0.03)	CA-2.2m (CAFOS)
55987.62	274.62	19.59 (0.12)	19.11 (0.02)	18.76 (0.02)	17.78 (0.01)	17.78 (0.01)	LT (RATCam)
55998.67	285.67	...	19.43 (0.02)	18.96 (0.02)	18.00 (0.01)	17.95 (0.01)	NOT (ALFOSC)
56008.66	295.66	...	19.40 (0.03)	19.10 (0.03)	18.06 (0.02)	18.14 (0.03)	LT (RATCam)
56014.51	301.51	20.28 (0.07)	19.65 (0.01)	19.24 (0.02)	18.26 (0.01)	18.22 (0.01)	NOT (ALFOSC)
56026.49	313.49	...	19.86 (0.02)	19.44 (0.02)	18.47 (0.01)	18.41 (0.02)	NOT (ALFOSC)
56043.59	330.59	20.76 (0.06)	20.15 (0.02)	19.78 (0.02)	18.72 (0.01)	18.72 (0.02)	NOT (ALFOSC)
56071.42	358.42	...	20.61 (0.02)	20.28 (0.04)	19.20 (0.02)	19.36 (0.03)	NOT (ALFOSC)
56087.43	374.43	...	20.86 (0.02)	20.48 (0.03)	19.45 (0.02)	19.62 (0.02)	NOT (ALFOSC)
56096.48	383.48	21.62 (0.10)	20.95 (0.03)	20.60 (0.04)	19.51 (0.02)	19.81 (0.03)	NOT (ALFOSC)
56115.44	402.44	...	21.26 (0.03)	20.96 (0.05)	19.91 (0.02)	20.18 (0.04)	NOT (ALFOSC)
56132.43	419.43	...	21.38 (0.06)	21.07 (0.06)	20.19 (0.03)	20.49 (0.05)	NOT (ALFOSC)
56133.40	420.40	...	21.55 (0.05)	21.13 (0.06)	20.19 (0.03)	...	NOT (ALFOSC)
56154.39	441.39	...	21.76 (0.05)	21.46 (0.06)	20.58 (0.04)	21.01 (0.08)	NOT (ALFOSC)
56180.37	467.37	...	22.30 (0.05)	21.82 (0.06)	20.90 (0.04)	...	NOT (ALFOSC)
56313.73	600.73	...	...	22.44 (0.10)	...	...	NOT (ALFOSC)
56353.50	640.50	...	...	23.02 (0.00)	...	22.58 (0.00)	HST (ACS)
56371.69	658.69	...	23.42 (0.32)	...	...	...	NOT (ALFOSC)
56397.64	684.64	...	...	23.20 (0.20)	...	...	NOT (ALFOSC)
56445.43	732.43	...	23.96 (0.50)	...	...	...	NOT (ALFOSC)

Table 4. Optical colour-corrected SDSS *u* and S-corrected SDSS *griz* magnitudes for SN 2011dh. Errors are given in parentheses. For completeness data for the first 100 days already published in E14a are included.

JD (+2400000) (d)	Phase (d)	*u* (mag)	*g* (mag)	*r* (mag)	*i* (mag)	*z* (mag)	Telescope (Instrument)
55716.47	3.47	15.90 (0.03)	15.08 (0.01)	14.68 (0.01)	14.80 (0.01)	14.76 (0.02)	LT (RATCam)
55717.46	4.46	16.01 (0.03)	14.80 (0.01)	14.38 (0.01)	14.61 (0.01)	14.58 (0.02)	LT (RATCam)
55718.53	5.53	...	14.44 (0.04)	14.06 (0.01)	14.27 (0.01)	...	LT (RATCam)
55720.44	7.44	15.39 (0.02)	13.97 (0.01)	13.53 (0.01)	13.73 (0.02)	13.87 (0.01)	LT (RATCam)
55721.44	8.44	15.09 (0.01)	13.78 (0.01)	13.33 (0.01)	13.52 (0.01)	13.64 (0.01)	LT (RATCam)
55722.44	9.44	...	13.59 (0.01)	13.18 (0.01)	13.35 (0.01)	13.49 (0.01)	LT (RATCam)
55723.41	10.41	14.82 (0.03)	...	13.02 (0.01)	13.16 (0.01)	13.34 (0.01)	LT (RATCam)
55724.41	11.41	14.72 (0.02)	...	12.93 (0.01)	13.05 (0.01)	13.22 (0.01)	LT (RATCam)
55725.43	12.43	14.74 (0.04)	...	12.83 (0.01)	12.94 (0.01)	13.09 (0.01)	LT (RATCam)
55729.39	16.39	14.56 (0.03)	13.10 (0.01)	12.56 (0.01)	12.62 (0.01)	12.81 (0.01)	LT (RATCam)
55730.40	17.40	14.45 (0.03)	13.07 (0.01)	12.51 (0.01)	12.56 (0.01)	12.77 (0.01)	LT (RATCam)
55731.41	18.41	14.54 (0.03)	13.02 (0.01)	12.46 (0.01)	12.51 (0.01)	12.71 (0.01)	LT (RATCam)
55731.82	18.82	...	13.07 (0.01)	12.46 (0.01)	12.50 (0.01)	12.65 (0.01)	FTN (FS02)
55732.46	19.46	14.56 (0.01)	13.00 (0.03)	12.42 (0.01)	12.48 (0.01)	12.67 (0.01)	LT (RATCam)
55733.45	20.45	14.52 (0.05)	13.03 (0.01)	12.41 (0.01)	12.45 (0.01)	12.65 (0.01)	LT (RATCam)
55735.44	22.44	14.75 (0.04)	13.12 (0.01)	12.43 (0.01)	12.41 (0.01)	12.60 (0.01)	LT (RATCam)
55736.44	23.44	14.96 (0.03)	13.19 (0.02)	12.45 (0.01)	12.42 (0.01)	12.59 (0.02)	LT (RATCam)
55738.45	25.45	15.37 (0.02)	13.43 (0.01)	12.55 (0.01)	12.47 (0.01)	12.65 (0.01)	LT (RATCam)
55739.44	26.44	15.55 (0.02)	13.50 (0.03)	12.59 (0.01)	12.50 (0.01)	12.65 (0.01)	LT (RATCam)
55740.44	27.44	15.80 (0.01)	13.66 (0.01)	12.66 (0.01)	12.55 (0.01)	12.70 (0.01)	LT (RATCam)
55741.44	28.44	...	13.75 (0.02)	12.76 (0.01)	12.59 (0.02)	12.76 (0.01)	LT (RATCam)
55742.49	29.49	16.20 (0.02)	13.92 (0.01)	12.84 (0.01)	12.65 (0.01)	12.80 (0.01)	LT (RATCam)
55745.44	32.44	16.71 (0.05)	14.20 (0.02)	13.04 (0.01)	12.79 (0.01)	12.87 (0.03)	LT (RATCam)
55745.80	32.80	...	14.35 (0.04)	13.00 (0.01)	12.79 (0.01)	12.94 (0.01)	FTN (FS02)
55746.45	33.45	16.83 (0.04)	14.32 (0.01)	13.09 (0.01)	12.82 (0.01)	12.94 (0.01)	LT (RATCam)
55747.44	34.44	16.90 (0.04)	14.40 (0.02)	13.13 (0.01)	12.86 (0.01)	12.95 (0.01)	LT (RATCam)
55748.44	35.44	17.09 (0.04)	14.42 (0.02)	13.19 (0.01)	12.90 (0.01)	13.01 (0.01)	LT (RATCam)
55750.44	37.44	17.20 (0.10)	14.55 (0.02)	13.29 (0.01)	13.02 (0.02)	13.04 (0.04)	LT (RATCam)
55751.43	38.43	17.14 (0.03)	14.64 (0.03)	13.36 (0.01)	13.04 (0.01)	13.11 (0.01)	LT (RATCam)
55752.45	39.45	17.24 (0.07)	14.66 (0.01)	13.39 (0.01)	13.04 (0.01)	13.09 (0.01)	LT (RATCam)
55756.46	43.46	...	14.79 (0.01)	13.55 (0.01)	13.22 (0.01)	13.19 (0.01)	LT (RATCam)
55762.78	49.78	...	15.00 (0.02)	13.68 (0.01)	13.37 (0.01)	13.28 (0.01)	FTN (FS02)
55767.43	54.43	17.30 (0.02)	15.03 (0.01)	13.84 (0.01)	13.52 (0.01)	13.38 (0.02)	LT (RATCam)
55768.45	55.45	17.29 (0.02)	15.03 (0.01)	13.86 (0.01)	13.56 (0.01)	13.41 (0.01)	LT (RATCam)
55773.39	60.39	17.27 (0.04)	15.07 (0.01)	13.99 (0.01)	13.72 (0.01)	13.54 (0.02)	NOT (ALFOSC)
55776.38	63.38	17.36 (0.03)	15.13 (0.01)	14.03 (0.01)	13.76 (0.01)	13.56 (0.01)	NOT (ALFOSC)
55780.41	67.41	17.33 (0.03)	15.16 (0.01)	14.09 (0.01)	13.84 (0.01)	13.61 (0.01)	NOT (ALFOSC)
55783.44	70.44	17.26 (0.04)	15.18 (0.01)	14.19 (0.01)	13.93 (0.01)	13.67 (0.01)	NOT (ALFOSC)
55784.77	71.77	...	15.23 (0.02)	14.16 (0.01)	13.88 (0.01)	13.64 (0.01)	FTN (FS02)
55790.38	77.38	17.29 (0.03)	15.35 (0.04)	14.28 (0.01)	14.04 (0.01)	13.69 (0.02)	LT (RATCam)
55793.37	80.37	17.32 (0.03)	15.30 (0.01)	14.39 (0.01)	14.16 (0.01)	13.84 (0.01)	NOT (ALFOSC)
55797.76	84.76	...	15.38 (0.01)	14.42 (0.01)	14.18 (0.01)	13.82 (0.01)	FTN (FS02)
55798.37	85.37	17.35 (0.03)	15.38 (0.01)	14.50 (0.01)	14.26 (0.01)	13.87 (0.01)	NOT (ALFOSC)
55801.36	88.36	17.34 (0.01)	15.42 (0.01)	14.53 (0.01)	14.31 (0.01)	13.89 (0.01)	NOT (ALFOSC)
55810.34	97.34	17.49 (0.02)	15.55 (0.01)	14.75 (0.01)	14.56 (0.01)	14.10 (0.02)	NOT (ALFOSC)
55886.75	173.75	21.74 (1.97)	16.99 (0.01)	16.36 (0.01)	16.16 (0.01)	...	NOT (ALFOSC)
55894.76	181.76	18.89 (0.03)	17.19 (0.02)	16.50 (0.01)	16.28 (0.02)	16.31 (0.02)	NOT (ALFOSC)
55898.73	185.73	18.97 (0.03)	17.25 (0.01)	16.59 (0.01)	16.42 (0.01)	16.49 (0.01)	NOT (ALFOSC)
55903.76	190.76	19.07 (0.05)	17.32 (0.02)	16.68 (0.01)	16.47 (0.01)	16.68 (0.04)	NOT (ALFOSC)
55912.79	199.79	19.28 (0.04)	17.48 (0.02)	16.86 (0.01)	16.66 (0.01)	16.79 (0.03)	NOT (ALFOSC)

Table 5. Continued.

JD (+2400000) (d)	Phase (d)	*u* (mag)	*g* (mag)	*r* (mag)	*i* (mag)	*z* (mag)	Telescope (Instrument)
55922.77	209.77	19.44 (0.02)	17.71 (0.01)	17.05 (0.01)	16.83 (0.01)	17.18 (0.01)	NOT (ALFOSC)
55932.79	219.79	19.50 (0.05)	17.83 (0.02)	17.18 (0.02)	17.01 (0.02)	17.37 (0.04)	NOT (ALFOSC)
55939.74	226.74	19.74 (0.05)	18.02 (0.01)	17.31 (0.01)	17.11 (0.01)	17.49 (0.02)	NOT (ALFOSC)
55948.73	235.73	19.87 (0.03)	18.15 (0.01)	17.45 (0.01)	17.27 (0.01)	17.74 (0.01)	NOT (ALFOSC)
55955.76	242.76	20.01 (0.03)	18.27 (0.01)	17.57 (0.01)	17.40 (0.01)	17.87 (0.02)	NOT (ALFOSC)
55975.69	262.69	20.37 (0.04)	18.64 (0.01)	17.84 (0.01)	17.71 (0.01)	18.25 (0.02)	NOT (ALFOSC)
55982.74	269.74	20.64 (0.05)	18.74 (0.01)	17.92 (0.01)	17.86 (0.01)	18.42 (0.03)	NOT (ALFOSC)
55987.62	274.62	20.47 (0.11)	18.76 (0.01)	17.95 (0.01)	17.96 (0.01)	18.30 (0.03)	LT (RATCam)
56008.66	295.66	...	19.14 (0.02)	18.22 (0.01)	18.33 (0.03)	19.27 (0.10)	LT (RATCam)
56014.52	301.52	21.28 (0.04)	19.30 (0.01)	18.40 (0.01)	18.45 (0.01)	19.02 (0.02)	NOT (ALFOSC)
56043.60	330.60	21.73 (0.03)	19.82 (0.01)	18.82 (0.01)	18.96 (0.01)	19.52 (0.03)	NOT (ALFOSC)
56071.43	358.43	21.85 (0.06)	20.27 (0.02)	19.26 (0.02)	19.62 (0.03)	19.98 (0.05)	NOT (ALFOSC)
56096.49	383.49	22.35 (0.05)	20.61 (0.02)	19.55 (0.02)	20.09 (0.03)	...	NOT (ALFOSC)
56132.43	419.43	...	21.14 (0.03)	20.21 (0.03)	20.79 (0.05)	21.25 (0.17)	NOT (ALFOSC)
56133.41	420.41	...	21.30 (0.04)	20.21 (0.03)	20.95 (0.06)	...	NOT (ALFOSC)
56154.39	441.39	...	21.50 (0.04)	20.61 (0.03)	21.32 (0.07)	...	NOT (ALFOSC)
56313.75	600.75	...	...	22.46 (0.11)	...	...	NOT (ALFOSC)
56428.46	715.46	...	...	23.10 (0.20)	...	...	NOT (ALFOSC)

Table 6. NIR S-corrected 2MASS *JHK* magnitudes for SN 2011dh. Errors are given in parentheses. For completeness data for the first 100 days already published in E14a are included.

JD (+2400000) (d)	Phase (d)	*J* (mag)	*H* (mag)	*K* (mag)	Telescope (Instrument)
55716.51	3.51	14.09 (0.01)	13.90 (0.01)	13.68 (0.02)	TNG (NICS)
55722.40	9.40	12.89 (0.01)	12.87 (0.01)	12.67 (0.01)	TNG (NICS)
55725.50	12.50	12.61 (0.04)	12.54 (0.01)	12.43 (0.02)	NOT (NOTCAM)
55730.51	17.51	12.12 (0.01)	12.08 (0.01)	11.94 (0.01)	TNG (NICS)
55737.72	24.72	11.96 (0.01)	11.90 (0.01)	11.72 (0.03)	LBT (LUCIFER)
55741.13	28.13	11.94 (0.01)	11.90 (0.02)	11.70 (0.05)	TCS (CAIN)
55748.43	35.43	12.14 (0.01)	12.00 (0.02)	11.77 (0.01)	TCS (CAIN)
55750.42	37.42	12.19 (0.01)	12.00 (0.01)	11.84 (0.04)	TCS (CAIN)
55751.42	38.42	12.29 (0.01)	12.01 (0.01)	11.84 (0.03)	TCS (CAIN)
55758.45	45.45	12.55 (0.01)	12.22 (0.01)	12.06 (0.01)	TNG (NICS)
55759.41	46.41	12.49 (0.03)	12.22 (0.03)	12.11 (0.04)	TCS (CAIN)
55762.41	49.41	12.57 (0.01)	12.26 (0.01)	12.17 (0.03)	TCS (CAIN)
55763.42	50.42	12.62 (0.02)	12.27 (0.04)	12.25 (0.06)	TCS (CAIN)
55765.45	52.45	12.79 (0.01)	12.38 (0.01)	12.23 (0.01)	TNG (NICS)
55769.41	56.41	12.77 (0.01)	12.48 (0.06)	12.40 (0.03)	TCS (CAIN)
55773.37	60.37	12.94 (0.03)	12.58 (0.01)	12.42 (0.02)	TNG (NICS)
55774.40	61.40	12.90 (0.01)	12.55 (0.03)	12.43 (0.04)	TCS (CAIN)
55776.40	63.40	13.00 (0.01)	12.64 (0.01)	12.53 (0.02)	TCS (CAIN)
55781.41	68.41	13.23 (0.01)	12.76 (0.01)	12.66 (0.01)	WHT (LIRIS)
55787.44	74.44	13.56 (0.03)	13.03 (0.02)	12.95 (0.02)	NOT (NOTCAM)
55801.36	88.36	13.90 (0.02)	13.41 (0.02)	13.17 (0.01)	TNG (NICS)
55804.34	91.34	14.10 (0.01)	13.50 (0.01)	13.26 (0.01)	CA-3.5m (O2000)
55814.32	101.32	14.38 (0.01)	13.80 (0.01)	13.50 (0.01)	CA-3.5m (O2000)
55818.36	105.36	14.45 (0.02)	13.91 (0.01)	13.74 (0.01)	NOT (NOTCAM)
55880.72	167.72	16.23 (0.01)	15.38 (0.01)	14.70 (0.01)	CA-3.5m (O2000)
55913.68	200.68	17.00 (0.01)	16.19 (0.02)	15.31 (0.02)	CA-3.5m (O2000)
55914.66	201.66	17.05 (0.01)	16.23 (0.02)	15.35 (0.02)	CA-3.5m (O2000)
55946.13	233.13	17.43 (0.02)	16.78 (0.02)	16.21 (0.02)	UKIRT (WFCAM)
55999.91	286.91	18.10 (0.02)	17.47 (0.02)	17.31 (0.02)	UKIRT (WFCAM)
56024.38	311.38	18.46 (0.03)	17.80 (0.03)	17.71 (0.04)	WHT (LIRIS)
56052.47	339.47	18.69 (0.02)	17.96 (0.02)	18.60 (0.03)	WHT (LIRIS)
56093.48	380.48	19.71 (0.06)	18.71 (0.06)	19.21 (0.08)	WHT (LIRIS)

Table 7. MIR Spitzer 3.6 μm and 4.5 μm magnitudes for SN 2011dh. Errors are given in parentheses. For completeness data for the first 100 days already published in E14a are included.

JD (+2400000) (d)	Phase (d)	3.6 μm (mag)	4.5 μm (mag)	Telescope (Instrument)
55731.21	18.21	11.83 (0.02)	11.48 (0.02)	SPITZER (IRAC)
55737.06	24.06	11.66 (0.02)	11.31 (0.02)	SPITZER (IRAC)
55744.32	31.32	11.66 (0.02)	11.30 (0.02)	SPITZER (IRAC)
55751.46	38.46	11.68 (0.02)	11.30 (0.02)	SPITZER (IRAC)
55758.75	45.75	11.79 (0.02)	11.32 (0.02)	SPITZER (IRAC)
55766.45	53.45	11.96 (0.02)	11.34 (0.02)	SPITZER (IRAC)
55772.33	59.33	12.11 (0.03)	11.38 (0.02)	SPITZER (IRAC)
55779.12	66.12	12.30 (0.03)	11.43 (0.02)	SPITZER (IRAC)
55785.60	72.60	12.50 (0.03)	11.50 (0.02)	SPITZER (IRAC)
55798.28	85.28	12.84 (0.04)	11.66 (0.03)	SPITZER (IRAC)
55964.14	251.14	14.34 (0.09)	13.31 (0.07)	SPITZER (IRAC)
56026.63	313.63	15.57 (0.15)	14.27 (0.11)	SPITZER (IRAC)
56104.23	391.23	17.12 (0.32)	15.54 (0.19)	SPITZER (IRAC)
56136.41	423.41	17.46 (0.37)	16.01 (0.24)	SPITZER (IRAC)
56168.69	455.69	17.63 (0.40)	16.25 (0.26)	SPITZER (IRAC)
56337.59	624.59	18.42 (0.57)	17.59 (0.49)	SPITZER (IRAC)

Table 8. List of late-time (100-415 days) optical and NIR spectroscopic observations.

JD (+2400000) (d)	Phase (d)	Grism	Range (Å)	Resolution	Resolution (Å)	Telescope (Instrument)
55821.33	108.33	b200	3300-8700	...	12.0	CA-2.2m (CAFOS)
55821.33	108.33	r200	6300-10500	...	12.0	CA-2.2m (CAFOS)
55828.35	115.35	R300B	3200-5300	...	4.1	WHT (ISIS)
55828.35	115.35	R158R	5300-10000	...	7.7	WHT (ISIS)
55830.25	117.25	Grism 4	3500-8450	613	...	AS 1.82m (AFOSC)
55864.65	151.65	Grism 4	3500-8450	613	...	AS 1.82m (AFOSC)
55867.71	154.71	?	?-?	...	?	CA-2.2m (CAFOS)
55893.76	180.76	Grism 3	3200-6700	345	12.4	NOT (ALFOSC)
55897.76	184.76	Grism 5	5000-10250	415	16.8	NOT (ALFOSC)
55911.20	198.20	zJ	8900-15100	700	...	WHT (LIRIS)
55914.70	201.70	R300B	3200-5300	...	8.2	WHT (ISIS)
55914.70	201.70	R158R	5300-10000	...	15.4	WHT (ISIS)
55918.69	205.69	HK	14000-25000	333	...	TNG (NICS)
55951.64	238.64	Grism 4	3200-9100	355	16.2	NOT (ALFOSC)
55998.68	285.68	r200	6300-10500	...	12.0	CA-2.2m (CAFOS)
56005.63	292.63	Grism 4	3200-9100	355	16.2	NOT (ALFOSC)
56013.14	300.14	R600B	?-?	...	5.7	WHT (ISIS)
56013.14	300.14	R316R	?-?	...	3.0	WHT (ISIS)
56071.56	358.56	R500B	3440-7600	322	15.0	GTC (OSIRIS)
56072.61	359.61	R500R	4800-10000	352	20.8	GTC (OSIRIS)
56128.47	415.47	R300B	3600-7000	270	16.7	GTC (OSIRIS)

Table 9. Pseudo-bolometric 3-300 days UV to MIR lightcurve for SN 2011dh calculated from spectroscopic and photometric data with a 1-day sampling between 3 and 50 days and a 5-day sampling between 50 and 300 days. Random errors are given in the first parentheses and systematic lower and upper errors (arising from the distance and extinction) respectively in the second parentheses.

JD (+2400000) (d)	Phase (d)	L (log erg s^{-1})	JD (+2400000) (d)	Phase (d)	L (log erg s^{-1})
55717.00	4.00	41.465 (0.001) (0.098,0.186)	55773.00	60.00	41.670 (0.002) (0.093,0.160)
55718.00	5.00	41.553 (0.001) (0.097,0.181)	55778.00	65.00	41.627 (0.002) (0.093,0.160)
55719.00	6.00	41.653 (0.001) (0.097,0.179)	55783.00	70.00	41.585 (0.002) (0.093,0.161)
55720.00	7.00	41.747 (0.001) (0.097,0.178)	55788.00	75.00	41.544 (0.002) (0.093,0.161)
55721.00	8.00	41.835 (0.001) (0.097,0.178)	55793.00	80.00	41.502 (0.002) (0.093,0.161)
55722.00	9.00	41.909 (0.001) (0.097,0.178)	55798.00	85.00	41.460 (0.002) (0.093,0.162)
55723.00	10.00	41.970 (0.001) (0.097,0.177)	55803.00	90.00	41.417 (0.002) (0.094,0.162)
55724.00	11.00	42.019 (0.001) (0.097,0.176)	55808.00	95.00	41.375 (0.002) (0.094,0.163)
55725.00	12.00	42.057 (0.001) (0.097,0.176)	55813.00	100.00	41.333 (0.002) (0.094,0.163)
55726.00	13.00	42.089 (0.001) (0.096,0.175)	55818.00	105.00	41.291 (0.002) (0.094,0.163)
55727.00	14.00	42.118 (0.001) (0.096,0.174)	55823.00	110.00	41.249 (0.001) (0.094,0.164)
55728.00	15.00	42.142 (0.001) (0.096,0.174)	55828.00	115.00	41.208 (0.001) (0.094,0.164)
55729.00	16.00	42.164 (0.001) (0.096,0.173)	55833.00	120.00	41.166 (0.001) (0.094,0.164)
55730.00	17.00	42.182 (0.001) (0.096,0.173)	55838.00	125.00	41.124 (0.001) (0.094,0.164)
55731.00	18.00	42.198 (0.001) (0.096,0.173)	55843.00	130.00	41.081 (0.002) (0.094,0.164)
55732.00	19.00	42.209 (0.001) (0.096,0.172)	55848.00	135.00	41.038 (0.002) (0.094,0.165)
55733.00	20.00	42.214 (0.001) (0.096,0.172)	55853.00	140.00	40.995 (0.001) (0.094,0.165)
55734.00	21.00	42.216 (0.001) (0.096,0.171)	55858.00	145.00	40.953 (0.001) (0.094,0.165)
55735.00	22.00	42.211 (0.001) (0.095,0.171)	55863.00	150.00	40.909 (0.001) (0.094,0.165)
55736.00	23.00	42.201 (0.001) (0.095,0.170)	55868.00	155.00	40.863 (0.001) (0.094,0.165)
55737.00	24.00	42.186 (0.001) (0.095,0.169)	55873.00	160.00	40.817 (0.001) (0.094,0.165)
55738.00	25.00	42.165 (0.001) (0.095,0.167)	55878.00	165.00	40.772 (0.001) (0.094,0.165)
55739.00	26.00	42.142 (0.001) (0.094,0.166)	55883.00	170.00	40.726 (0.001) (0.094,0.164)
55740.00	27.00	42.117 (0.001) (0.094,0.165)	55888.00	175.00	40.681 (0.001) (0.094,0.164)
55741.00	28.00	42.091 (0.001) (0.094,0.164)	55893.00	180.00	40.637 (0.001) (0.094,0.164)
55742.00	29.00	42.064 (0.001) (0.094,0.163)	55898.00	185.00	40.594 (0.001) (0.094,0.164)
55743.00	30.00	42.039 (0.001) (0.094,0.162)	55903.00	190.00	40.552 (0.001) (0.094,0.164)
55744.00	31.00	42.016 (0.001) (0.093,0.162)	55908.00	195.00	40.512 (0.001) (0.094,0.164)
55745.00	32.00	41.996 (0.001) (0.093,0.161)	55913.00	200.00	40.472 (0.001) (0.094,0.164)
55746.00	33.00	41.977 (0.001) (0.093,0.161)	55918.00	205.00	40.432 (0.001) (0.094,0.164)
55747.00	34.00	41.959 (0.001) (0.093,0.160)	55923.00	210.00	40.396 (0.001) (0.094,0.164)
55748.00	35.00	41.943 (0.001) (0.093,0.160)	55928.00	215.00	40.362 (0.001) (0.094,0.164)
55749.00	36.00	41.928 (0.001) (0.093,0.160)	55933.00	220.00	40.327 (0.001) (0.094,0.164)
55750.00	37.00	41.914 (0.001) (0.093,0.159)	55938.00	225.00	40.294 (0.001) (0.094,0.164)
55751.00	38.00	41.900 (0.001) (0.093,0.159)	55943.00	230.00	40.262 (0.001) (0.094,0.164)
55752.00	39.00	41.887 (0.001) (0.093,0.159)	55948.00	235.00	40.230 (0.001) (0.094,0.164)
55753.00	40.00	41.874 (0.001) (0.093,0.159)	55953.00	240.00	40.200 (0.001) (0.094,0.163)
55754.00	41.00	41.861 (0.001) (0.093,0.159)	55958.00	245.00	40.169 (0.001) (0.094,0.163)
55755.00	42.00	41.848 (0.001) (0.093,0.159)	55963.00	250.00	40.137 (0.001) (0.094,0.163)
55756.00	43.00	41.836 (0.001) (0.093,0.159)	55968.00	255.00	40.104 (0.001) (0.094,0.163)
55757.00	44.00	41.823 (0.001) (0.093,0.159)	55973.00	260.00	40.071 (0.001) (0.094,0.163)
55758.00	45.00	41.812 (0.001) (0.093,0.159)	55978.00	265.00	40.039 (0.001) (0.094,0.163)
55759.00	46.00	41.802 (0.001) (0.093,0.159)	55983.00	270.00	40.006 (0.001) (0.094,0.163)
55760.00	47.00	41.792 (0.001) (0.093,0.159)	55988.00	275.00	39.973 (0.001) (0.094,0.163)
55761.00	48.00	41.782 (0.001) (0.093,0.159)	55993.00	280.00	39.940 (0.001) (0.094,0.163)
55762.00	49.00	41.773 (0.002) (0.093,0.159)	55998.00	285.00	39.907 (0.001) (0.094,0.163)
55763.00	50.00	41.763 (0.002) (0.093,0.159)	56003.00	290.00	39.873 (0.001) (0.094,0.163)
55768.00	55.00	41.716 (0.002) (0.093,0.159)	56008.00	295.00	39.838 (0.001) (0.094,0.163)